UNIVERSITÉ GRENOBLE ALPES

INTERNSHIP REPORT

Modeling and Control of a PEM Fuel Cell Stack

Author:
Khalil Ellah LAGHA

Supervisor:
Prof. Emmanuel WITRANT

Infinity Team - Gipsa

October 22, 2026

Declaration of Authorship

I, Khalil Ellah LAGHA, declare that this thesis titled, “Modeling and Control of a PEM Fuel Cell Stack” and the work presented in it are my own. I confirm that:

- This work was done wholly or mainly while in candidature for a research degree at this University.
- Where any part of this thesis has previously been submitted for a degree or any other qualification at this University or any other institution, this has been clearly stated.
- Where I have consulted the published work of others, this is always clearly attributed.
- Where I have quoted from the work of others, the source is always given. With the exception of such quotations, this thesis is entirely my own work.
- I have acknowledged all main sources of help.
- Where the thesis is based on work done by myself jointly with others, I have made clear exactly what was done by others and what I have contributed myself.

Signed:

Date:

"Where there is a will there's a way."

George Herbert

UNIVERSITÉ GRENOBLE ALPES

Abstract

Modeling and Control of a PEM Fuel Cell Stack

by Khalil Ellah LAGHA

This report presents the modeling, calibration, and dynamic characterization of a proton exchange membrane fuel cell (PEMFC) stack carried out at GIPSA-lab. A simplified control-oriented model is developed from electrochemical principles: a Nernst open-circuit voltage combined with semi-empirical activation, ohmic, and concentration corrections is distinguished from the analytical gas and water balances. Six coefficients per cell are fitted to the Optimization Experiment using differential evolution followed by L-BFGS-B, with calibration voltage RMSE below 12 mV for cells 3–9. Their physical interpretation is limited by non-identifiability and the implemented activation-sign convention. A separate two-coefficient empirical model predicts a withheld chronological block with RMSE of 1.8–10.2 mV; this remains a same-run check using measured inputs. The state-space analysis shows that hydrogen inlet flow alone controls only the pressure state and that voltage alone cannot observe the full three-state model. Pressure observability in the reduced model requires known or fixed hydration. Step-load datasets labelled 3.3 and 6.8 Ω give fitted current time constants of approximately 8–10 s, with sensitivity to the fitting interval and unresolved current calibration. A full operating-cycle experiment records sequential loss of cell voltage and a supply-recovery fit of $\tau_s \approx 151$ s. These observations motivate a proposed DC/DC boost converter with PI regulation of stack current or output voltage. Bench-specific gains and closed-loop performance remain to be established. Derivations, parameter tables, and additional processing checks are provided in the appendices.

Acknowledgements

I would like to thank my supervisor, Prof. Emmanuel Witrant, and the Infinity Team at GIPSA-lab for their guidance and support throughout this internship.

Contents

Declaration of Authorship ii

Abstract iv

Acknowledgements v

1 Introduction 1

2 Context & Background 3
2.1 Host Laboratory and Research Context . . . 3
2.2 Operating Principle of a PEM Fuel Cell . . . 3
2.3 Voltage Losses and Polarization Behavior . . . 3
2.4 State of the Art . . . 4
2.4.1 Practical Challenges and Choice of Control Strategy . . . 4
2.5 Hydrogen Safety and the Operating Environment . . . 5

3 Methodology 6
3.1 Simplified Control-Oriented Model . . . 6
3.1.1 Open-Circuit Voltage . . . 6
3.1.2 Voltage Losses . . . 6
3.1.3 Anode Dynamics . . . 7
3.1.4 Membrane and Cathode . . . 7
3.1.5 Model Properties and Next Steps . . . 7
3.2 Per-Cell Parameter Identification . . . 7
3.3 State-Space Representation, Controllability and Observability . . . 9
3.3.1 State-Space Representation . . . 9
3.3.2 Controllability . . . 10
3.3.3 Observability . . . 10
3.4 Experimental Protocols . . . 11

4 Results & Analysis 12
4.1 Parameter Identification on the Optimization Experiment . . . 12
4.1.1 Chronological Holdout Check . . . 12
4.2 Step-Response Characterization (TR-Current Experiments) . . . 13
4.3 Full Operating-Cycle Experiments (July 2026) . . . 15
4.3.1 Start-Up and Valve Test . . . 15
4.3.2 The Five Phases of the Loaded Cycle . . . 15
4.3.3 Sequential Cell Collapse during Fuel Depletion . . . 16
4.3.4 Supply-Side Response Time . . . 16
4.3.5 Open-Circuit Operation and the Absence of Charge Storage . . . 16

5 Control of the PEMFC Power System: DC/DC Boost Converter with PI Controller 21
5.1 System Overview . . . 21
5.2 Stack-Current Regulation . . . 21
5.3 Output Voltage Regulation (Voltage-Source Operation) . . . 23

6 Conclusion & Perspectives **24**

A Derivation of the Open-Circuit Voltage **27**

B Detailed Tables **29**

C Source Code **30**

D Additional Processing and Prediction Checks **31**
D.1 Per-Cell Calibration and Reconstruction 31
D.2 Calibration and Reconstruction Windows 31
D.3 Chronological Holdout 31
D.4 Current-Response Fits and Measurement Provenance 33
D.5 Reproducibility 33

List of Figures

1.1 Experimental bench 2

2.1 Operating principle and structure of a PEM fuel cell 4
2.2 Voltage losses and polarization curve 5

3.1 Block-level architecture of the simplified PEMFC model 8
3.2 Differential-evolution convergence per cell 9

4.1 Stack voltage and load current, Optimization Experiment 13
4.2 TR-current step experiments 14
4.3 Current step response and exponential fit 15
4.4 Start-up and valve test 18
4.5 Full operating-cycle experiment 19
4.6 Order of cell collapse during fuel depletion 20
4.7 Current response to supply reopening 20

5.1 Proposed control architecture of the PEMFC power system 22

D.1 Per-cell voltage–current calibration fits 32
D.2 Per-cell voltage: measured vs. reconstructed 32
D.3 Chronological holdout for cells 3–9 34

List of Tables

3.1 Optimization variables for the per-cell identification 8

4.1 Chronological prediction errors of the empirical comparison model. The final block is not used to fit a_k, b_k. 13
4.2 Current step-response metrics 14
4.3 Phases of the full operating-cycle experiment 16

A.1 Gibbs free energy change of the hydrogen fuel cell reaction at various temperatures [11]. . . . 27

B.1 Fitted coefficients and calibration RMSE 29

D.1 Calibration error and full-loaded-interval reconstruction error using the original fitted coefficients. Reconstruction includes the excluded transient. 31

List of Abbreviations

PEMFC	**P**roton **E**xchange **M**embrane **F**uel **C**ell
MEA	**M**embrane **E**lectrode **A**ssembly
OCV	**O**pen-**C**ircuit **V**oltage (stack voltage with no load connected)
RMSE	**R**oot-**M**ean-**S**quare **E**rror
DE	**D**ifferential **E**volution (global optimizer)
L-BFGS-B	**L**imited-memory **B**royden–**F**letcher–**G**oldfarb–**S**hanno algorithm with **B**ound constraints (local optimizer)
TR	*Temps de Réponse*: French for "response time"; label of the load-step campaign
PRBS	**P**seudo-**R**andom **B**inary **S**equence (test excitation signal)
DAQ	**D**ata **Acq**uisition
PI	**P**roportional–**I**ntegral (controller)
PWM	**P**ulse-**W**idth **M**odulation
DC/DC	**D**irect-**C**urrent to **D**irect-**C**urrent (voltage converter)
LQ	**L**inear–**Q**uadratic (optimal control)

Chapter 1

Introduction

Fuel cells convert the chemical energy of hydrogen directly into electricity, with water and heat as the only by-products. Among them, the proton exchange membrane fuel cell (PEMFC) is the leading candidate for transport and small stationary applications thanks to its low operating temperature, high power density, and fast start-up [11, 3]. Their efficient and safe operation, however, requires feedback control of the gas supply and load: insufficient reactant flow causes starvation and irreversible degradation, while excessive anode–cathode pressure difference can damage the membrane [20, 8]. Control design, in turn, requires a model that is simple enough for analysis and accurate enough to represent the actual hardware, including the differences between individual cells of a stack [1].

This internship, carried out at GIPSA-lab (Université Grenoble Alpes) under the supervision of Prof. Emmanuel Witrant, addresses this need for a small educational PEMFC stack of ten cells. The objectives are:

1) to develop a simplified, control-oriented dynamic model of a single cell and of the stack, grounded in the electrochemical literature;

2) to identify the model parameters *per cell* from experimental data acquired on the bench;

3) to derive the linearized state-space representation and analyze its structural controllability and observability, as a foundation for controller and observer design;

4) to characterize experimentally the dynamic response of the stack to resistive load steps, providing the timescales needed for control bandwidth selection;

5) to propose a PI-based control architecture for the PEMFC power system through a DC/DC boost converter, following [4].

All the experimental work was carried out on the instrumented PEMFC bench shown in Figure 1.1. Hydrogen is stored in a metal-hydride canister (1) and admitted to the stack through a pressure regulator (2) and a proportional solenoid valve (4); a flow sensor (3, Honeywell AWM42) and pressure sensors (5, MPX4250DP; 6, relative) instrument the hydrogen circuit. The heart of the bench is a ten-cell EDUSTAK JUNIOR stack (7), loaded by interchangeable power resistors (8, $25/3.3/6.8\,\Omega$) and mounted on a base that carries the data-acquisition electronics (9). A serial acquisition chain developed during the project records every individual cell voltage, the pressures, the hydrogen flows, and the stack current at 1 Hz, so that each experiment produces a complete, per-cell picture of the stack. Because hydrogen is a highly flammable gas, the bench is operated in a ventilated room under the strict environmental precautions discussed in Section 2.5.

The report is organized to give a global vision of the work. Chapter 2 summarizes the operating principle of PEMFCs, positions the work in the literature, and explains the practical constraints that shaped the control strategy. Chapter 3 presents the simplified model, the parameter-identification procedure, the linearized state-space analysis, and the experimental protocols. Chapter 4 discusses the calibration and step-response results. Chapter 5 presents the control of the PEMFC power system with a DC/DC boost converter and a PI controller. Chapter 6 concludes and outlines perspectives. The open-circuit-voltage derivation and the full per-cell parameter table are provided in Appendices A and B; the main text is self-contained and readable without them. All the software produced during the internship (the simplified

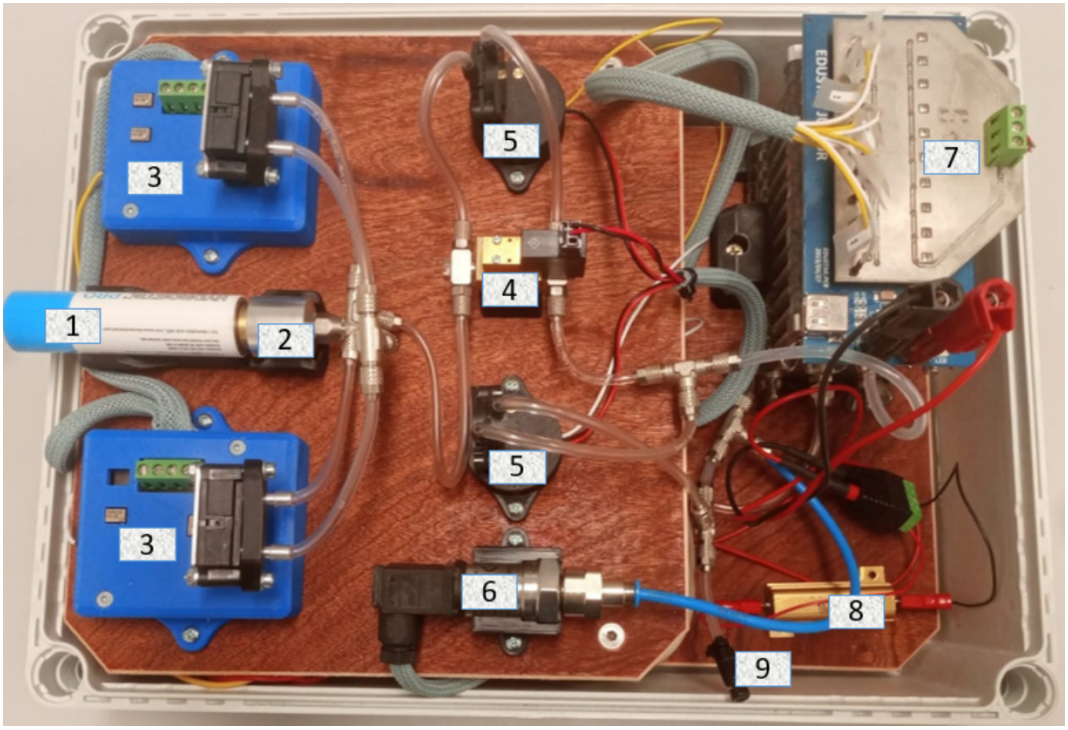


FIGURE 1.1: The instrumented PEMFC bench used throughout this work: (1) metal-hydride H_2 storage, (2) pressure regulator, (3) flow sensor, (4) proportional solenoid valve, (5)–(6) pressure sensors, (7) ten-cell EDUSTAK JUNIOR stack, (8) load resistors, (9) mounting and acquisition base.

model, the parameter-identification and figure-generation scripts, and the LaTeX sources of this report and of the defense presentation) is openly available on GitHub,[1] as detailed in Appendix C.

[1] https://github.com/KhalilEllahLAGHA/PEMFC_Internship_codes

Chapter 2

Context & Background

2.1 Host Laboratory and Research Context

The internship was carried out at GIPSA-lab, a joint research laboratory of CNRS, Grenoble INP–UGA, and Université Grenoble Alpes. Its theoretical and applied research covers automatic control, signal and image processing, speech, cognition, robotics, and learning [6]. The internship supervisor, Prof. Emmanuel Witrant, leads the Infinity team, which develops modeling, estimation, and control methods for distributed systems, including systems described by partial differential equations and delays [5]. The present work addresses a smaller, lumped-parameter model of an educational PEMFC stack. It connects this control-oriented research environment with bench measurements, parameter identification, and the practical constraints of an experimental energy system.

2.2 Operating Principle of a PEM Fuel Cell

A proton exchange membrane fuel cell (PEMFC) converts the chemical energy of hydrogen and oxygen directly into electricity, heat, and water [1, 10, 14]. At the anode, hydrogen splits into protons and electrons. The protons cross the polymer membrane, while the electrons travel through the external circuit and supply the load. At the cathode, oxygen recombines with both to form water (Figure 2.1). The overall reaction is

$$\mathrm{H_2} + \tfrac{1}{2}\mathrm{O_2} \rightarrow \mathrm{H_2O} + \text{electricity} + \text{heat}.$$

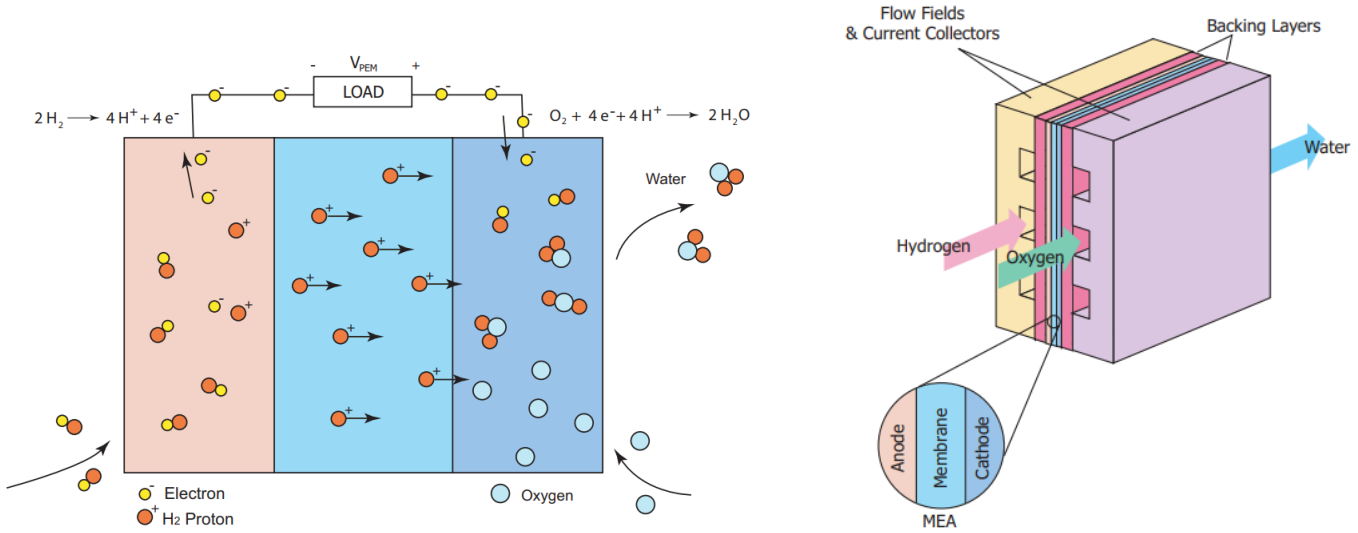
The membrane conducts protons, blocks electrons, and separates fuel from oxidant. Together with the two electrodes it forms the membrane electrode assembly (MEA), the elementary repeating unit of the stack [1, 7]. Water management is critical to performance: a dry membrane loses proton conductivity, whereas excess liquid water floods the gas channels. Stable operation therefore requires a balance between hydration and drainage [18, 19].

2.3 Voltage Losses and Polarization Behavior

A practical cell delivers less than its reversible voltage because of three loss mechanisms, each dominant in a different region of the polarization curve (Figure 2.2) [1, 11, 13]:

- **activation loss**: the kinetic penalty of driving the electrode reactions, dominant at low current [11, 18];
- **ohmic loss**: the resistive drop across the membrane and conductors, approximately linear in current [11, 13];
- **concentration loss**: the mass-transport limitation that causes the steep voltage drop at high current [1, 18].

The *polarization curve* is the cell voltage plotted against current density; it is the fingerprint of cell performance and the basis for the model of Chapter 3. Fast transients are further shaped by the charge double-layer at the electrode/electrolyte interface, which behaves as a small capacitor in equivalent-circuit models [11, 1].



(A) Electrochemical operation: hydrogen oxidation at the anode, proton transport through the membrane, oxygen reduction at the cathode.

(B) Stack structure: individual MEAs stacked in series to add their voltages.

FIGURE 2.1: Operating principle and physical structure of a PEM fuel cell. A single cell delivers roughly one volt, so cells are stacked in series to reach a useful voltage [10, 14, 1].

2.4 State of the Art

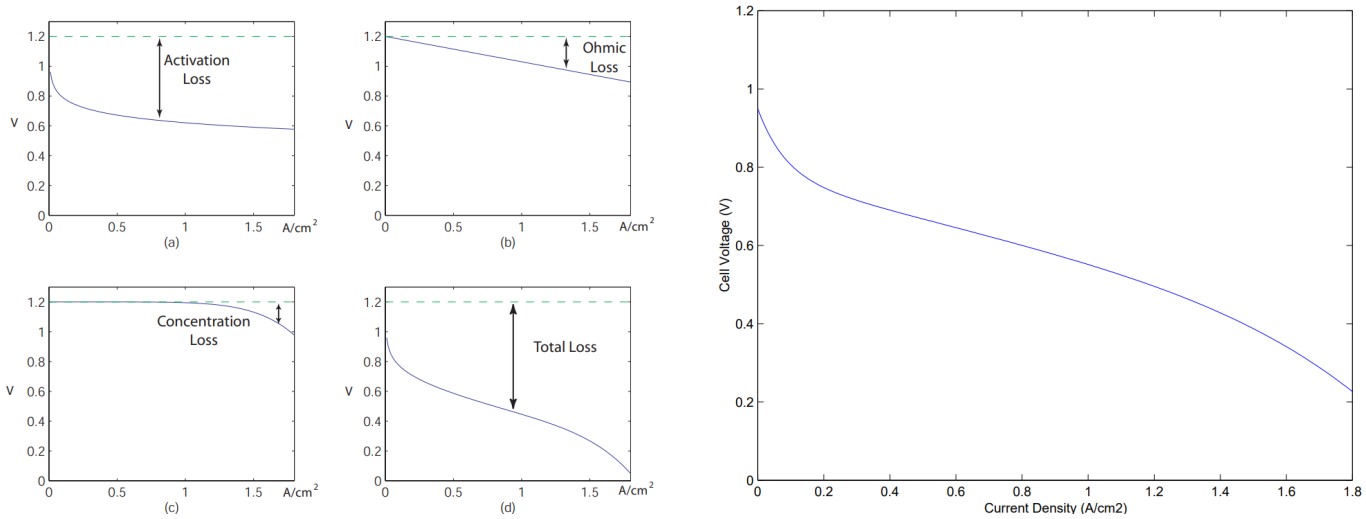
Control-oriented PEMFC modeling traces back to the system-level model of Pukrushpan [11], which couples a polarization-curve voltage law with compressor, manifold-filling, and membrane-hydration dynamics; later control-oriented models specialize or simplify this approach [13, 9, 20]. Simplified electrical models reproduce the static voltage–current characteristic of small stacks with only a handful of parameters [1, 12]. Crucially, per-cell measurements on a small stack reveal voltage deviations of up to 7 % between cells [1], which motivates the per-cell calibration adopted here. Parameter identification by direct-search optimization on measured voltage and power was used by Thanapalan et al. [13] and extended with modern metaheuristics [2].

On the control side, proportional–integral (PI) regulation of flows, pressures, and converter currents is the established baseline [20, 4]. Documented upgrades include linear-quadratic (LQ) multivariable control, time-delay control, and model-predictive schemes [11, 9, 17]. At system level, the response delays of the air and hydrogen supply components can limit dynamic operation [8].

2.4.1 Practical Challenges and Choice of Control Strategy

The control strategy of this work was shaped directly by constraints observed on the laboratory bench. The hydrogen supply maintains reactant availability: raising the anode hydrogen partial pressure increases the Nernst voltage logarithmically, while the current drawn is primarily set by the electrical load. In practice, the usable hydrogen pressure on the educational stack is narrowly bounded. The supply regulator caps the inlet pressure, and a large anode–cathode pressure difference risks mechanical damage to the thin membrane [20, 8]. The pressure can therefore be varied only within a small range, which yields too little authority to regulate the operating point across the full load. Direct current control through the hydrogen valve was explored and found impractical for the same reason: the actuator saturates before the load demand is met.

This limitation motivated the chosen approach. The proposed control acts on the electrical side: the stack would feed a DC/DC boost converter whose duty cycle is set by a PI loop [4]. The converter adapts the stack voltage to the load and controls the current drawn from the cells, while the gas supply maintains adequate reactant availability. It does not remove the stack's power and reactant-supply limits: a rapid increase in electrical demand must still respect the available gas flow and cell-voltage limits. This separation



(A) Decomposition into activation, ohmic, and concentration losses.

(B) Resulting polarization curve.

FIGURE 2.2: Influence of the three loss mechanisms on PEMFC performance. Activation dominates at low current, ohmic loss in the middle, and concentration loss near the limiting current; together they bend the ideal flat voltage into the characteristic polarization curve.

of roles (electrical regulation coordinated with gas-supply constraints) underlies the architecture proposed in Chapter 5.

2.5 Hydrogen Safety and the Operating Environment

Working with hydrogen imposes a discipline on the experimental environment that is an integral part of operating any fuel-cell system, and it deserves to be stated explicitly: hydrogen is a flammable gas, and the environment in which it is handled must be strictly controlled. Hydrogen is flammable over an exceptionally wide range of concentrations in air (roughly 4–75 % by volume), and its minimum ignition energy (of the order of 0.02 mJ) is about an order of magnitude below that of common hydrocarbon fuels, so even a weak electrostatic discharge can ignite a flammable mixture. Hydrogen leaks require particular attention to fittings, seals, and material compatibility. It burns with a pale blue flame that is nearly invisible in daylight, which makes an incipient fire difficult to detect [15].

These properties translate into strict rules for the room and the procedures, not only for the bench. All the experiments of this work were performed in a *continuously ventilated room*. Hydrogen is much lighter than air and tends to rise, but can still accumulate in poorly ventilated or enclosed spaces. Ventilation helps disperse a leak; its presence alone does not establish that the concentration stays below the lower flammability limit. Ventilation, leak detection, appropriate materials, and trained handling are complementary measures [16, 15]. The operating precautions reported for this bench include leak checks before operation, limiting the supply pressure to that required by the experiment, keeping ignition sources away from the bench, and closing the storage canister with the line depressurized whenever the bench is unattended. The shutdown and depressurization sequence must follow the laboratory-approved procedure. The environment must be controlled and monitored as carefully as the experiment itself; the precautions described here do not constitute a complete safety assessment of the installation.

The same discipline protects the stack as much as the operator. An over-pressurized anode can mechanically damage the thin membrane [20, 8], while operating on a starved supply degrades the electrodes. Pressure regulation must therefore be accompanied by adequate reactant flow and appropriate current limits. The voltage deterioration discussed in Chapter 4 reinforces the need to monitor individual cells, without by itself establishing a unique degradation mechanism.

Chapter 3

Methodology

3.1 Simplified Control-Oriented Model

Following [13, 11], the cell is split into three interacting parts (anode, membrane, and cathode), each lumped into a single control volume. The main assumptions are: hydrogen and air are the only reactants; channel pressure drops are neglected; gases obey the ideal-gas law; temperature is constant or slowly varying; and the oxygen partial pressure is fixed at $P^*_{O_2} = 0.21\,P_{\text{atm}}$. The result is a simplified semi-empirical model: physically motivated mass balances combined with empirical voltage terms calibrated from data [2]. The voltage calibration and the dynamic analysis are separate parts of the work: the experimental fit below evaluates an algebraic voltage law, while the gas and water balances provide an analytical framework whose dynamics have not been independently validated.

3.1.1 Open-Circuit Voltage

The reversible voltage, an ideal reference for open-circuit operation, follows from the Gibbs free energy of the reaction and Faraday's law (full derivation in Appendix A):

$$E = 1.229 - 0.85 \times 10^{-3}(T_{fc} - 298.15) + 4.31 \times 10^{-5}\, T_{fc} \left[\ln p_{H_2} + \tfrac{1}{2} \ln p_{O_2}\right] \ \text{V}, \tag{3.1}$$

with T_{fc} the stack temperature [K] and p_{H_2}, p_{O_2} the reactant partial pressures [atm] [11].

3.1.2 Voltage Losses

The cell voltage is the reversible voltage minus the three losses of Section 2.3:

$$v_{fc} = E - v_{act} - v_{ohm} - v_{con}, \tag{3.2}$$

with the following forms retained from the calibration implementation, inspired by the semi-empirical literature [11, 13, 2]:

$$v_{act} = \xi_1 + \xi_2 T + \xi_3 T \ln(C_{O_2}) + \xi_4 T \ln(i_{FC}), \tag{3.3}$$

$$v_{ohm} = i_{FC}\left(\rho_m \frac{t_m}{A_{fc}} + c\right), \qquad \rho_m = \left[(b_{11}\lambda_m - b_{12}) \exp\left(b_2\left(\tfrac{1}{303.15} - \tfrac{1}{T_{fc}}\right)\right)\right]^{-1}, \tag{3.4}$$

$$v_{con} = -B \ln\left(1 - \frac{i_{FC}}{i_{\max}}\right), \tag{3.5}$$

where i_{FC} is the cell current, C_{O_2} the dissolved-oxygen concentration (Henry's law), t_m and A_{fc} the membrane thickness and active area, λ_m the membrane water content, and $\boldsymbol{\theta} = (\xi_1, \xi_2, \xi_3, \xi_4, B, c)$ the six coefficients fitted per cell in Section 3.2. The implementation uses $b_{11} = 0.5139\,\text{S}\,\text{m}^{-1}$, $b_{12} = 0.326\,\text{S}\,\text{m}^{-1}$, and $b_2 = 1268\,\text{K}$. The stack voltage is the sum over the n cells in series.

With the implemented bound $\xi_4 \leq 0$, $\partial v_{act}/\partial i_{FC} = \xi_4 T / i_{FC} \leq 0$. This is therefore a *local empirical correction*, not a validated increasing activation loss. The equation and fits retain the implemented convention; changing its sign requires recalibration. The logarithmic law is restricted to $0 < i_{FC} < i_{\max}$ and the

measured interval, without extrapolation to open circuit or interpretation as an equilibrium polarization curve.

3.1.3 Anode Dynamics

The hydrogen pressure follows a mass balance on the anode volume with Faraday consumption:

$$\dot{P}_{H_2} = \frac{R_{H_2} T}{V_{an}} \left(W_{H_2,in} - W_{H_2,out} - \frac{M_{H_2} n}{2F} i_{FC} \right), \tag{3.6}$$

Here the volumes and mass flows refer to the whole stack, consistently with the factor n in reactant consumption. With SI mass-balance units, P_{H_2} is an absolute pressure in Pa; the Nernst expression uses $p_{H_2} = P_{H_2}/101325$. The anode water balance keeps only the membrane flux, $\dot{m}_{w,an} = W_{v,mbr}$, with relative humidity $\phi_{an} = m_{w,an} R_v T / (V_{an} p_{sat}(T))$. The hydrogen pressure P_{H_2} enters the Nernst term of (3.1) and is the primary state of interest.

3.1.4 Membrane and Cathode

Water crosses the membrane by electro-osmotic drag (protons dragging water molecules from anode to cathode) and by back-diffusion. To match the anode balance, $W_{v,mbr} > 0$ denotes net transport *from cathode to anode*. Using the current i_{FC} in amperes and current density $j = i_{FC}/A_{fc}$, the net stack mass flow is written consistently as [11]

$$W_{v,mbr} = n M_v A_{fc} \frac{D_w}{t_m} (c_{v,ca} - c_{v,an}) - \frac{n M_v n_d}{F} i_{FC}, \tag{3.7}$$

where $c_{v,an}$ and $c_{v,ca}$ are the membrane-face water concentrations [mol m^{-3}], D_w is a membrane diffusion coefficient [m^2 s^{-1}], and n_d is the number of water molecules transported per proton. The area factor cancels in the drag term because i_{FC} is a current, not a current density. The membrane water content follows the Springer sorption isotherm $\lambda(a) = 0.043 + 17.81a - 39.85a^2 + 36.0a^3$, averaged over the two faces for water activities within the isotherm's range. On the cathode side, the oxygen partial pressure is held at $P^*_{O_2} = 0.21\, P_{\text{atm}}$, which removes the oxygen state while keeping the cathode water balance, $\dot{m}_{w,ca} = -W_{v,mbr} + W_{v,gen}$ with $W_{v,gen} = M_v n\, i_{FC}/(2F)$, whose humidity feeds back into the ohmic loss through λ_m. The block-level architecture of the resulting model is shown in Figure 3.1.

3.1.5 Model Properties and Next Steps

The state vector is $\mathbf{x} = (P_{H_2}, m_{w,an}, m_{w,ca})$. Current is a load-imposed disturbance, hydrogen inlet flow is the manipulated input, and cell voltage is the output. The constant-P_{O_2} assumption and lumped volumes keep the order low, while omitting spatial gradients, oxygen transients, and liquid-water accumulation [18, 19]. The following sections distinguish voltage calibration from structural dynamic analysis and experimental response characterization; the fitted errors do not validate gas and water dynamics.

3.2 Per-Cell Parameter Identification

The six coefficients of each cell are fitted by minimizing the root-mean-square error (RMSE) between predicted and measured cell voltage over a calibration window:

$$\min_{\boldsymbol{\theta}} \sqrt{\frac{1}{N} \sum_{i=1}^{N} \left(v_{\text{model}}(I_i, P_{H_2,i}; \boldsymbol{\theta}) - v_{\text{meas},i} \right)^2}. \tag{3.8}$$

The implementation fixes $T = 343.15\,\text{K}$, $p_{O_2} = 0.21\,\text{atm}$, and $\lambda_m = 14$; these are assumed calibration conditions rather than identified states. It also uses $A_{fc} = 25 \times 10^{-4}\,\text{m}^2$, $t_m = 178 \times 10^{-6}\,\text{m}$, and $i_{\max} = 0.25\,\text{A}$. The loaded window contains 549 samples from $t = 135$ to 683 s. Its first 164 samples are excluded

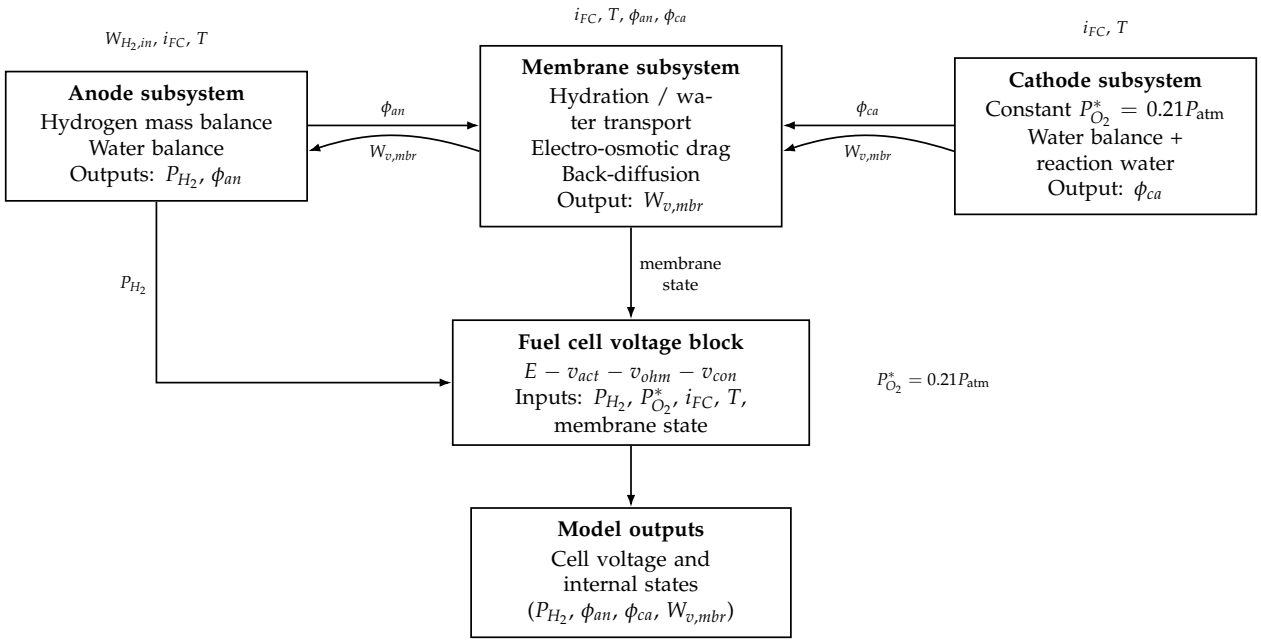


FIGURE 3.1: Block-level architecture of the simplified PEMFC model. The anode, membrane, and cathode subsystems exchange water and feed the voltage block, which combines the Nernst potential with the three losses to produce the cell voltage. The diagram makes explicit which signals are inputs (top) and which are internal states.

TABLE 3.1: Decision variables of the per-cell identification problem (3.8), with their role in the loss equations (3.3)–(3.5) and the search bounds. The four ξ coefficients shape the empirical activation term; B and c scale the concentration and contact-resistance losses.

Variable	Role in the voltage law	Unit	Search bounds
ξ_1	Activation: constant term (3.3)	V	$[-8.0,\ 2.0]$
ξ_2	Activation: temperature term	$\mathrm{V\,K^{-1}}$	$[0,\ 3\times10^{-2}]$
ξ_3	Activation: oxygen-concentration term	$\mathrm{V\,K^{-1}}$	$[-5\times10^{-3},\ 5\times10^{-3}]$
ξ_4	Activation: current term (≤ 0)	$\mathrm{V\,K^{-1}}$	$[-1\times10^{-2},\ 0]$
B	Concentration-loss coefficient (3.5)	V	$[0,\ 2.0]$
c	Contact / lumped ohmic resistance (3.4)	Ω	$[0,\ 1\times10^{-2}]$

and 80 approximately uniformly spaced samples from $t = 299$ to 683 s are retained, covering reconstructed currents of about 16.00–25.84 mA. Current is calculated as $i_{FC} = V_{stack}/25\,\Omega$ and pressure is supplied from the measured channel; the fit does not predict either input dynamically.

At fixed T and C_{O_2}, the first three coefficients enter only through

$$\theta_0 = \xi_1 + T\xi_2 + T\ln(C_{O_2})\xi_3. \tag{3.9}$$

Thus at most (θ_0, ξ_4, B, c) can be distinguished structurally, with further practical ambiguity over the narrow current interval. The six fitted coefficients are not unique physical estimates. Since current also comes from the measured voltage, the residuals quantify local reconstruction rather than independent predictive validation.

Table 3.1 lists the decision variables and the box bounds used by the optimizer. The constraints $B \geq 0$ and $c \geq 0$ keep their respective loss contributions non-negative over the fitted current range. The bound $\xi_4 \leq 0$ reproduces the implemented empirical convention; it does not enforce increasing activation loss.

A two-stage strategy is used: **differential evolution** for the global search (population multiplier 20, up to 800 generations, fixed seed 42), followed by **L-BFGS-B** local refinement under the same bounds. Differential evolution is a population-based optimizer that needs no gradient; L-BFGS-B then polishes the best candidate. With the other quantities fixed here, voltage is affine in the fitted coefficients, so the

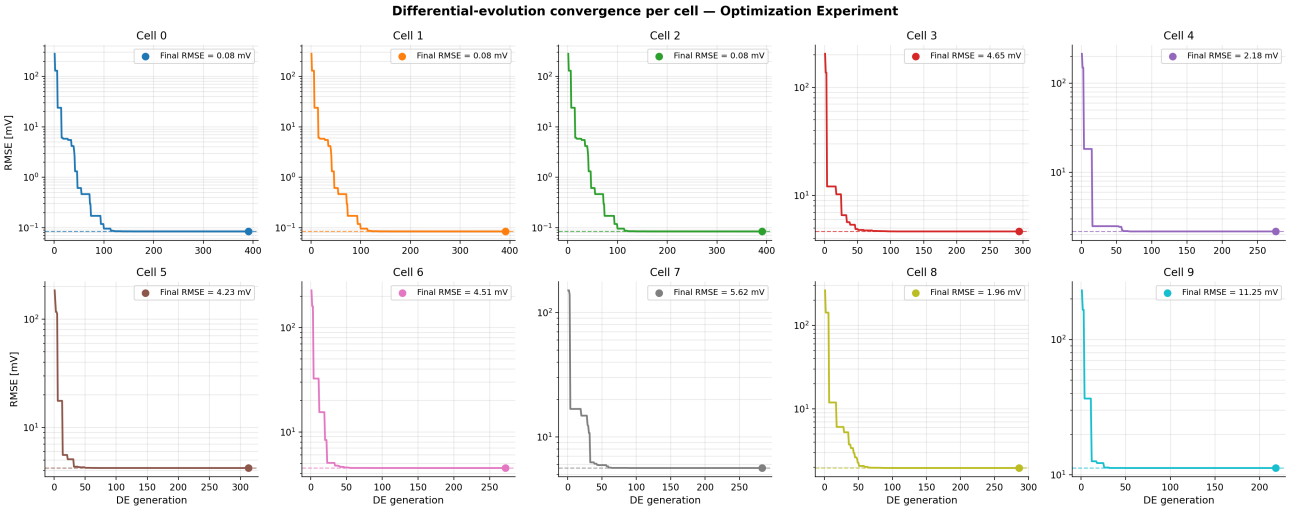


FIGURE 3.2: Differential-evolution convergence (RMSE versus generation, log scale) for the ten cells. The dashed line marks the final RMSE after L-BFGS-B refinement. Most cells converge within a few tens of generations; the degraded cells (0–2) collapse almost immediately to a near-zero RMSE against a flat zero-voltage signal, which is the first sign of a degenerate fit.

bounded least-squares problem is convex but rank deficient. A global search is therefore not required for this particular calibration. The convergence plot (Figure 3.2) documents the procedure used, without establishing unique physical parameters.

3.3 State-Space Representation, Controllability and Observability

To prepare for control and observer design, perturbations about a nominal trajectory $(\mathbf{x}_0(t), \mathbf{u}_0(t))$ are considered. With coefficients frozen at a selected condition, the local model is written as $\delta\dot{\mathbf{x}} = A\delta\mathbf{x} + B\delta\mathbf{u}$, $\delta y = C\delta\mathbf{x} + D\delta\mathbf{u}$. Controllability is assessed through the rank of $\mathcal{C} = [B\ AB\ A^2B]$ and observability through $\mathcal{O} = [C; CA; CA^2]$.

3.3.1 State-Space Representation

The linearized model uses the state, input, and output vectors

$$\mathbf{x} = \begin{bmatrix} P_{H_2} \\ m_{w,an} \\ m_{w,ca} \end{bmatrix}, \qquad \mathbf{u} = \begin{bmatrix} i_{FC} \\ W_{H_2,in} \end{bmatrix}, \qquad y = v_{fc},$$

where current remains a disturbance and inlet flow the manipulated input. A describes internal dynamics, B the input effects, C voltage sensitivities to states, and D direct input-to-voltage feedthrough.

Matrices A and B: a frozen transport approximation

The hydrogen pressure balance (3.6), with $W_{H_2,out} \approx 0$ for the dead-end anode, is linear at fixed temperature. The membrane transport is generally nonlinear because sorption, diffusion, and drag depend on hydration. For the structural analysis here, an additional constant-coefficient approximation to (3.7) is introduced:

$$\delta W_{v,mbr} \approx -\beta\,\delta m_{w,an} + \gamma\,\delta m_{w,ca} - \frac{n n_d M_v}{F}\,\delta i_{FC}.$$

The effective $\beta, \gamma > 0$ [s^{-1}] absorb area, diffusion, and local concentration-to-mass sensitivities, rather than simply equaling $D_w/(Vt_m)$. Freezing temperature and n_d, define $d_1 = -nn_dM_v/F$ and $d_2 = nM_v(1/2 +$

$n_d)/F$ [kg C^{-1}]. This corrected analytical approximation has not been fitted to the voltage data. The perturbation matrices are

$$A = \begin{bmatrix} 0 & 0 & 0 \\ 0 & -\beta & \gamma \\ 0 & \beta & -\gamma \end{bmatrix}, \qquad B = \begin{bmatrix} -\dfrac{R_{H_2} T\, M_{H_2}\, n}{2F\, V_{an}} & \dfrac{R_{H_2} T}{V_{an}} \\ d_1 & 0 \\ d_2 & 0 \end{bmatrix}. \tag{3.10}$$

The first column of B is the effect of the load current (hydrogen consumption and electro-osmotic water displacement); the second column shows that the inlet flow acts on the hydrogen pressure only.

The underlying water balances give $\dot{m}_{w,an} + \dot{m}_{w,ca} = nM_v i_{FC}/(2F)$. Thus without water outlets or phase-change removal they have no fixed equilibrium at nonzero current. The frozen matrices describe local perturbations along a nominal trajectory, not a validated steady loaded operating point. Long-term predictions require the missing water-removal mechanisms and parameter validation.

Matrices C and D: obtained by Jacobian linearization

The nonlinear voltage law requires a Jacobian, $C = \partial v_{fc}/\partial \mathbf{x}$ and $D = \partial v_{fc}/\partial \mathbf{u}$, evaluated at the nominal condition. Pressure enters through the Nernst term; water enters through $m_w \to \phi \to \lambda_m \to \sigma_m \to v_{ohm}$. With $\sigma_m = 1/\rho_m$, define $\kappa_0 = i_0 t_m b_{11} \exp[b_2(1/303.15 - 1/T)]/(A_{fc}\sigma_{m,0}^2)$ and $\lambda'(a) = 17.81 - 79.70a + 108a^2$. The resulting matrices are

$$C = \begin{bmatrix} \dfrac{4.31 \times 10^{-5}\, T}{P_{H_2,0}} & \kappa_0\, \lambda'(\phi_{an,0})\, \dfrac{R_v T}{2V_{an} p_{sat}(T)} & \kappa_0\, \lambda'(\phi_{ca,0})\, \dfrac{R_v T}{2V_{ca} p_{sat}(T)} \end{bmatrix}, \tag{3.11}$$

$$D = \begin{bmatrix} -\left(\dfrac{\xi_4 T}{i_0} + \rho_{m,0}\dfrac{t_m}{A_{fc}} + c + \dfrac{B}{i_{\max} - i_0}\right) & 0 \end{bmatrix}. \tag{3.12}$$

In the simplified model where λ_m is held constant, the two water-state entries of C vanish and $C_{\text{red}} = \begin{bmatrix} 4.31 \times 10^{-5}\, T/P_{H_2,0} & 0 & 0 \end{bmatrix}$.

3.3.2 Controllability

With current treated as the load-imposed disturbance, the manipulated input is hydrogen inlet flow. Its input vector is

$$B_h = \begin{bmatrix} R_{H_2} T/V_{an} & 0 & 0 \end{bmatrix}^\top, \qquad AB_h = 0, \qquad \operatorname{rank}[B_h\ AB_h\ A^2 B_h] = 1. \tag{3.13}$$

Hydrogen flow controls the pressure state, but cannot independently control the water states in this approximation.

If a converter also manipulated current independently, the ideal two-input pair (A, B) would instead be assessed. For its water block A_w and $B_w = [d_1\ d_2]^\top$, $\det[B_w\ A_w B_w] = (d_1 + d_2)(\beta d_1 - \gamma d_2)$. Full mathematical controllability requires this expression to be nonzero. The corrected signs $d_1 \le 0$, $d_2 > 0$, and $d_1 + d_2 = nM_v/(2F) > 0$ ensure this for $\beta, \gamma > 0$ and $n_d \ge 0$. Actual bench controllability also depends on converter dynamics, input limits, and operating constraints.

3.3.3 Observability

With voltage as the only measurement, let $C = [c_p\ c_a\ c_c]$ from (3.11), with $c_p > 0$. Direct multiplication gives

$$CA = (c_c - c_a)\begin{bmatrix} 0 & \beta & -\gamma \end{bmatrix}, \qquad CA^2 = -(\beta + \gamma)CA. \tag{3.14}$$

Hence rank $\mathcal{O} \le 2$: the three-state frozen model is **not fully observable from voltage alone**. Its rank is two when $c_a \ne c_c$ and one when $c_a = c_c$. An unobservable zero mode combines pressure with the conserved water mode, so unknown hydration can obscure pressure as well.

If hydration is fixed and known, the output reduces to C_{red}: voltage observes pressure but not the water states. A pressure-only voltage observer therefore requires known current, temperature, oxygen pressure, hydration, and calibrated voltage terms. These statements concern the frozen linear approximation; they do not establish nonlinear observability along a varying trajectory or a validated observer.

3.4 Experimental Protocols

All experiments were performed on the ten-cell educational PEMFC stack of the laboratory bench, with per-cell voltage acquisition at 1 Hz through the serial data-acquisition chain developed in the project.

- **Optimization Experiment** (April 2026): a fixed 25 Ω resistor is connected at $t = 135$ s and removed at $t = 684$ s, with no valve-driven current control. The calibration points used for the per-cell parameter identification are drawn from the loaded window of this experiment.
- **TR-current step experiments** (9 June 2026): here "TR" stands for *temps de réponse*, French for "response time." The stack is left at open circuit, then a fixed resistor (3.3 Ω for Experiment 1, 6.8 Ω for Experiment 4) is connected at $t = 0$. The processing pipeline detects a jump greater than 100 on the recorded current scale. The 3.3 Ω record starts at that jump; the 6.8 Ω record starts at the selected current peak within the next 15 samples. The current relaxation is fitted with the exponential model $I(t) = I_{\text{ss}} + \Delta I\, e^{-t/\tau_I}$, from which settling times $T_{s,p\%} = -\tau_I \ln(p/100)$ are derived analytically relative to the fitted amplitude and asymptote.
- **Start-up and valve test** (7 July 2026): starting from a fully depleted, idle stack at open circuit, the supply regulator is opened at $t = 37$ s and the proportional solenoid valve is then driven fully open (22 V) between $t = 186$ s and $t = 283$ s. The run checks the response of the admission chain (regulator $\rightarrow$ valve $\rightarrow$ stack) and characterizes the open-circuit-voltage recovery of each cell.
- **Full operating-cycle experiment** (7 July 2026): the stack, holding only residual hydrogen, is connected to a fixed resistive load at $t = 114$ s and kept loaded for almost three hours. The hydrogen supply is reopened once at $t = 1559$ s and then left to deplete completely. The run traverses five operating phases (rest, starvation under load, refuelling, loaded operation on a depleting supply, and final starvation) and is analyzed in Section 4.3.

All channels of the acquisition chain are logged in every run: the ten cell voltages, the hydrogen-circuit pressures, the mass flows, the stack current, and the valve command. The July current channel has an uncalibrated open-circuit offset of about 237 counts on the script's mA scale; this value is not a calibration of the earlier runs. Absolute current values require verified gain and offset. A constant offset cancels in step amplitudes, whereas drift or gain error can still affect the estimated response metrics.

Chapter 4

Results & Analysis

4.1 Parameter Identification on the Optimization Experiment

The two-stage optimizer of Section 3.2 fitted the six coefficients for all ten cells from the loaded window of the Optimization Experiment. The complete set of tuned values is given in Appendix B, Table B.1. For the healthy cells the calibration RMSE ranges from 2.0 to 11.3 mV (below 12 mV in every case) and the mean time-series RMSE over cells 3–9 is 10.5 mV over the full loaded window. The 8.0 mV average over all ten channels is lower because it includes the near-zero channels. These errors describe reconstruction of this experiment; they do not establish the accuracy of the individual physical parameters or validate the gas and water dynamics.

Figure 4.1 places the experiment in context. The stack sits at its open-circuit plateau of about 4.57 V, falls initially to 1.92 V when the assumed 25 Ω resistor is connected at $t = 135$ s, and subsequently falls below 0.8 V before recovering when the resistor is removed at $t = 684$ s. The reconstructed load current starts at 76.9 mA and decreases to about 16 mA. Summing the ten cell predictions gives a loaded-window stack RMSE of 45.5 mV. The calculation uses measured pressure and $I = \sum_k v_{k,\mathrm{meas}}/25\,\Omega$ as inputs, so the agreement is a same-run algebraic reconstruction rather than a free-running stack simulation.

The per-cell calibration fits in Appendix D, Figure D.1, explain these numbers. Two findings stand out. First, the fitted law describes cells 3–9 over the calibration interval, while the concentration (B) and contact-resistance (c) terms stay close to zero. Over this narrow interval, this means that these terms are not required by the fit; it does not establish their physical absence or identify the loss mechanisms separately. The activation coefficients are also non-unique, as discussed in Section 3.2. Second, the measurements flag abnormal cell responses. Cells 0, 1, and 2 approach 0 V under load, and the optimizer returns identical parameter sets with RMSE below 0.1 mV on their settled calibration samples. Such fits result from cancellation of model terms and carry no physical interpretation. Electrode degradation, reactant distribution, and the acquisition channels would need separate checks before assigning a cause. Here "healthy" is only the operational classification used for cells 3–9 in this experiment.

The time-series comparison in Appendix D, Figure D.2, extends the reconstruction to the full loaded interval, including the transient excluded from calibration. Cells 7 and 9 have the largest loaded-window errors, 31.7 and 16.1 mV respectively; the other active cells range from 3.6 to 7.5 mV. The open-circuit overlay uses an additional fitted effective temperature (811–1468 K across the cells), which is an empirical offset parameter and not the physical stack temperature. Its agreement cannot be used to validate the loaded model or a start-up model.

4.1.1 Chronological Holdout Check

To test prediction beyond the fitted samples, the 385 settled samples are split chronologically: 269 samples from $t = 299$ to 567 s are used for fitting, and 116 samples from $t = 568$ to 683 s are withheld. A two-coefficient empirical comparison is used instead of assigning separate physical meanings to non-identifiable activation coefficients:

$$\widehat{v}_k = E(P_{H_2}) - a_k - b_k \ln\left(\frac{I}{0.02\,\mathrm{A}}\right) - R_m I, \qquad R_m = 0.00636594\,\Omega. \tag{4.1}$$

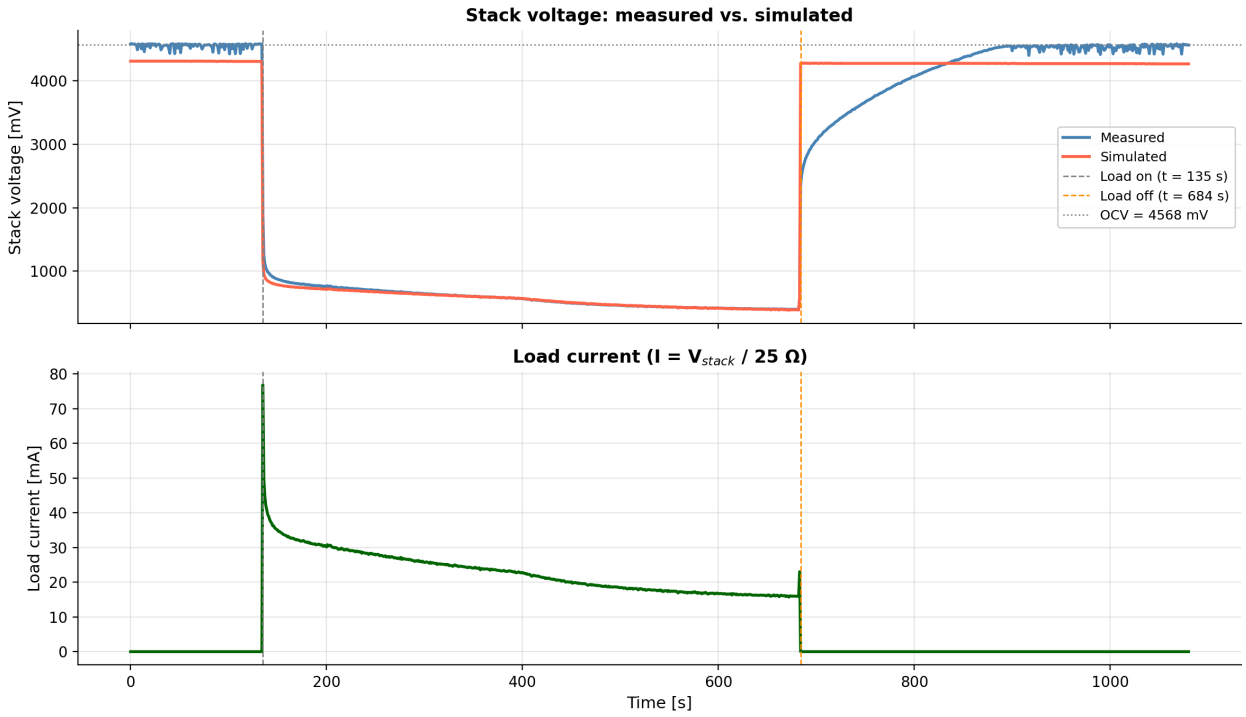


FIGURE 4.1: Stack voltage and load current during the Optimization Experiment. **Top:** measured (blue) and simulated (red) stack voltage; the load is applied at $t = 135\,\mathrm{s}$ and removed at $t = 684\,\mathrm{s}$. **Bottom:** the load current $I = V_{\mathrm{stack}}/25\,\Omega$. The loaded trace is reconstructed using measured inputs. The red open-circuit segments use a separate empirical effective-temperature fit; they are not predictions of the six loaded-model coefficients.

Here R_m is fixed from the original membrane constants, and a_k, b_k are obtained by least squares using the training block only. The training and holdout currents span 16.92–25.88 and 15.72–23.04 mA respectively.

TABLE 4.1: Chronological prediction errors of the empirical comparison model. The final block is not used to fit a_k, b_k.

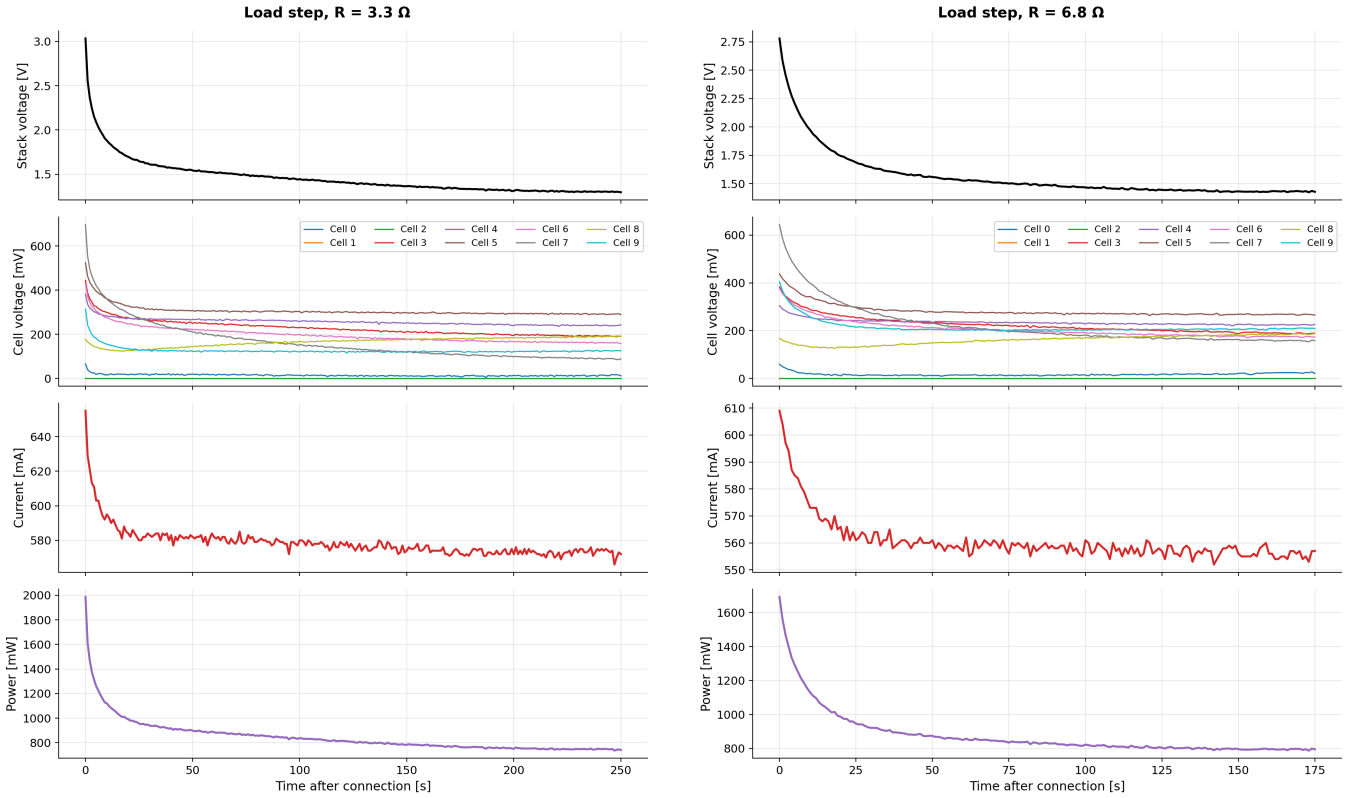
Cell	3	4	5	6	7	8	9
Training RMSE [mV]	1.68	1.33	1.57	1.62	1.81	1.24	1.36
Holdout RMSE [mV]	3.92	2.11	3.62	3.83	7.08	1.80	10.20

The held-out errors are larger, especially for cells 7 and 9, but remain below 10.3 mV. This supports limited chronological prediction within this run, using measured inputs. It does not validate independent gas or water dynamics, and the current still depends on the measured stack voltage. The full comparison and processing checks are provided in Appendix D.

4.2 Step-Response Characterization (TR-Current Experiments)

The TR-current experiments characterize how fast the stack current settles after a load step. In both runs, Cells 1 and 2 read about 0 mV throughout the loaded window, consistent with the abnormal response seen in the Optimization Experiment. Figure 4.2 shows the recorded channels for the datasets labelled 3.3 and 6.8 Ω. These labels are retained from the experiment files. Their physical load values and the current-channel gain and offset require verification; the following current values retain the scripts' mA scale (Appendix D).

Fitting the first-order model $I(t) = I_{\mathrm{ss}} + \Delta I\, e^{-t/\tau_I}$ to the current gives the metrics of Table 4.2, illustrated in Figure 4.3. The fitted asymptote and amplitude are used consistently in the curve and settling band. The



(A) Experiment 1, $R = 3.3\,\Omega$.

(B) Experiment 4, $R = 6.8\,\Omega$.

FIGURE 4.2: TR-current step experiments after resistor connection (time re-zeroed to the step): stack voltage, individual cell voltages, current, and power. Both signals relax toward a slowly varying level. A first-order fit summarizes the initial current relaxation, while residual drift remains. Current and power scales depend on the unresolved current calibration.

ideal settling time is defined relative to the fitted amplitude, $|I - I_{ss}| \leq 0.02|\Delta I|$; it is not a measured time after which every noisy sample remains inside the band.

TABLE 4.2: Current step-response metrics for the two labelled datasets. Levels and amplitudes are fitted values on the recorded current scale. The last row shows sensitivity to restricting the fit to the first 60 s.

Current metric	**Exp 1 (3.3 Ω)**	**Exp 4 (6.8 Ω)**
Fitted asymptote I_{ss} [mA]	576.4	557.7
Fitted amplitude ΔI [mA]	61.5	48.0
Time constant τ_I [s]	8.2	10.3
Settling time $T_{s,2\%}$ [s]	32.0	40.2
Fit RMSE [mA]	3.78	2.08
Time constant, first 60 s [s]	4.98	8.66

The whole-record fits give $\tau_I = 8.2$ and 10.3 s and ideal settling times of 32–40 s. Restricting the fit to the first 60 s changes the time constants to 5.0 and 8.7 s, showing sensitivity to the fitting interval and the remaining drift. The fitted values summarize these particular relaxations; they do not isolate an electrochemical mechanism or establish a load-dependent trend from two runs. A constant sensor offset would be absorbed by the fitted asymptote, but offset drift could affect the time constant. These timescales inform the control proposal of Chapter 5; converter dynamics, reactant availability, and stability margins must also determine the chosen bandwidth.

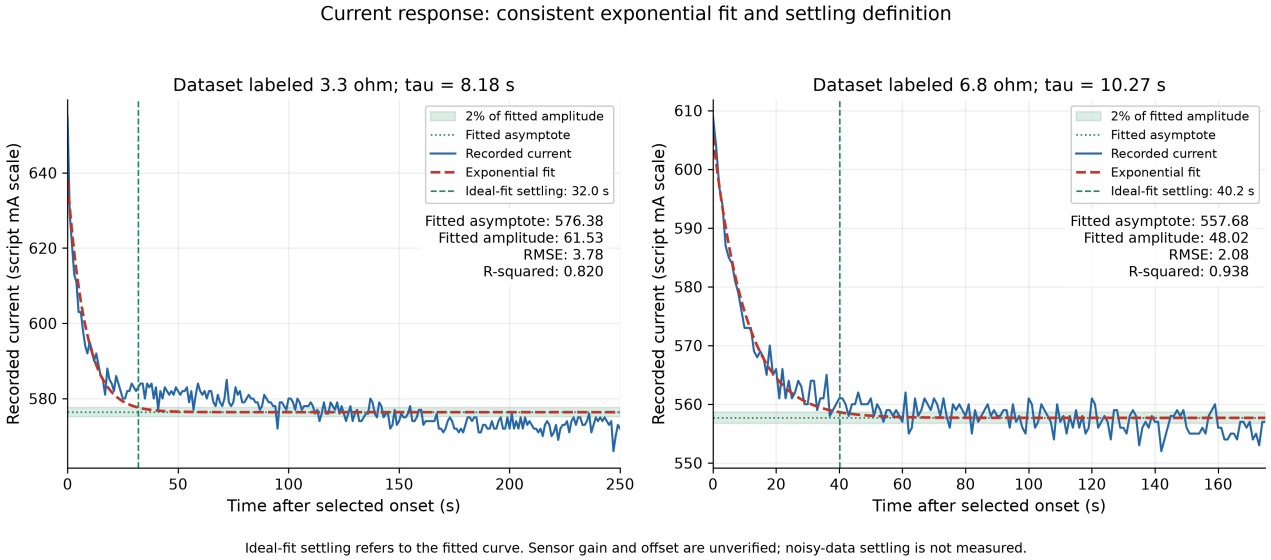


FIGURE 4.3: Current step response for the two loads: measured current (color), exponential fit (dashed), steady-state level, ±2 % settling band, and the 2 % settling time. The exponential model summarizes the relaxation, with residual drift; fit metrics are reported in Table 4.2. The band is centred on the fitted asymptote and has half-width $0.02|\Delta I|$; the vertical line is the ideal fitted settling time.

4.3 Full Operating-Cycle Experiments (July 2026)

Two complementary runs recorded on 7 July 2026 extend the step-response characterization to a complete operating cycle, from a cold start to total fuel exhaustion. Beyond response times, they expose the situations a controller must manage in practice: fuel starvation under load, recovery after refuelling, and the progressive collapse of the weakest cells.

4.3.1 Start-Up and Valve Test

Figure 4.4 shows the short start-up run, divided into four stages. Opening the supply regulator alone (stage B, supply line at about 56 kPa from $t = 37$ s) produces *no* cell response for 150 s: with the solenoid valve closed, no hydrogen reaches the stack, confirming that the valve (not the regulator) governs gas admission. Driving the valve fully open at $t = 186$ s (stage C) fills the anode within seconds; the supply line shows a transient spike to about 120 kPa before the regulator settles, and the first cells build voltage immediately. After the valve closes at $t = 283$ s (stage D), the anode pressure decays over about 90 s as the trapped hydrogen is consumed and redistributed, while the cells keep drifting up toward their open-circuit values for several minutes. The slow, staggered recovery of the open-circuit voltage (OCV, the stack voltage with no load connected) is consistent with recovery after depletion. The run checks the response of the valve and recorded channels ahead of the long experiment, without providing an independent sensor calibration or uniquely identifying the cause of the voltage drift.

4.3.2 The Five Phases of the Loaded Cycle

The main run lasts 2 h 57 min under a fixed resistive load and traverses the five phases summarized in Table 4.3 and displayed in Figure 4.5. In Phase I the stack rests at a residual open-circuit plateau of 1.93 V, left over from the start-up test. The load is connected at $t = 114$ s (Phase II) together with a brief hydrogen injection: the current channel steps up by 315 counts on its uncalibrated scale, then decays as the small amount of hydrogen trapped in the anode is consumed; the anode overpressure returns to zero within 15 minutes and the cells starve one after the other, the stack falling below 0.1 V. Reopening the supply at $t = 1559$ s (Phase III) revives the stack within minutes: the hydrogen-circuit differential pressure rises to about 70 kPa, the mass flow to its maximum, and the current recovers to a peak of 748 counts on the

recorded current scale. From there the supply is left to deplete (Phase IV): pressures and flows decline almost linearly for 86 minutes while the stack voltage and recorded current follow, and the weaker cells collapse in sequence. When the flow reaches zero at $t \approx 121$ min (Phase V), the two strongest cells continue to run on the hydrogen trapped in the anode volume for almost another hour before the stack dies completely.

TABLE 4.3: The five phases of the full operating-cycle experiment. The current channel is uncalibrated, with an open-circuit offset of about 237 counts.

Phase	Interval [min]	Duration	Stack [V]	What happens
I	0–1.9	2 min	1.93	rest, residual OCV
II	1.9–26	24 min	$1.29 \rightarrow 0.04$	load ON; starvation on trapped H_2
III	26–34.6	9 min	$0.42 \rightarrow 2.02$	supply reopened; recovery
IV	34.6–121	86 min	$2.02 \rightarrow 0.48$	loaded, supply depleting
V	121–177	56 min	$0.48 \rightarrow 0$	flows at zero; final starvation

4.3.3 Sequential Cell Collapse during Fuel Depletion

The order in which the cells lose voltage (Figure 4.6) is an empirical ranking obtained *during this operating cycle*, consistent with the abnormal responses flagged in Section 4.1. It may reflect cell condition, local reactant distribution, and hydration; it is not an independent measurement of intrinsic cell health. Cells 0–2, already flagged by their low loaded voltages, collapse within seconds of the load connection and never recover, even when fuel is available at the supply in Phases III–IV. The remaining cells then lose voltage in sequence as hydrogen runs out: 5, 6, and 4 during the depletion phase, then cell 8 at 129 min, and finally cell 9, which survives alone for almost half an hour on residual hydrogen and expires at 158 min.

One observation stands out: cell 7, which sustained voltage in the Optimization Experiment (calibration RMSE 5.6 mV), collapsed only seven minutes into the loaded starvation phase and did not recover after refuelling, unlike its neighbors. This behavior is consistent with an adverse effect of starvation, but the voltage record alone does not establish irreversible damage, cell reversal, or its cause. Repeated adequately fuelled tests and checks of the gas distribution and acquisition channel are needed to distinguish these explanations. The observation nevertheless reinforces the need to coordinate load demand with reactant availability.

4.3.4 Supply-Side Response Time

The supply reopening at $t = 1559$ s constitutes a natural step experiment on the *gas-supply side*, complementary to the resistor steps of Section 4.2 which excite the *load side*. Fitting the first-order model $I(t) = I_{ss} - \Delta I\, e^{-t/\tau_s}$ to the current recovery between the reopening and the current peak (Figure 4.7) gives a supply-side time constant

$$\tau_s \approx 151\,\text{s}, \qquad T_{s,2\%} \approx 592\,\text{s},$$

roughly **fifteen to twenty times longer** than the whole-record load-side fits ($\tau_I \approx 8$–10 s). This comparison supports investigating an electrical inner loop with slower supply supervision, consistent with [8]. The experiments use different initial conditions and excitation, however, so the ratio is not a measured universal separation of independent subsystems. The recovery segment lasts 516 s, shorter than the 592 s ideal settling time; the latter is an extrapolation of the fit, not an observed settling event. Neither this fit nor the resistor steps determine the duty-cycle-to-current transfer function needed to tune the converter PI loop.

4.3.5 Open-Circuit Operation and the Absence of Charge Storage

A recurring feature of both July runs is that the stack spent significant time at *open circuit*, supplied with hydrogen but with no load connected (all of Run 0 and Phase I of Run 1). A small recorded current in the tail of Run 1 does not by itself establish that the load was disconnected. In the open-circuit intervals the

cells settle toward their open-circuit voltage (OCV), the voltage measured across the stack when no current is drawn. It is worth being precise about what this residual voltage does, and does not, represent, because it bears directly on how the bench should be operated.

A PEM fuel cell is an *energy converter*: it converts the chemical energy of reactants into electrical power. Residual hydrogen can sustain generation after the inlet closes, and double-layer capacitance can store a small amount of electrical energy, but the observed OCV is not evidence that the stack has been charged like a battery. It is primarily the electrochemical potential set by the reactant gases still present at the electrodes (the Nernst term of Appendix A); as those residual gases are consumed or leak away, the OCV decays, exactly as observed in the slow post-valve drift of the start-up test and in the residual 1.93 V plateau at the beginning of Run 1.

The experiments do not establish that open-circuit operation caused the observed cell anomalies, nor do they justify a universal rule to connect the load before admitting hydrogen. A start-up or shutdown sequence must follow the stack manufacturer's guidance and the laboratory-approved procedure. The supported control conclusion is narrower: load demand must remain compatible with reactant availability, and low cell voltages must be monitored during operation. This links the supply-management observations to the proposed electrical control architecture without inferring an untested operating procedure.

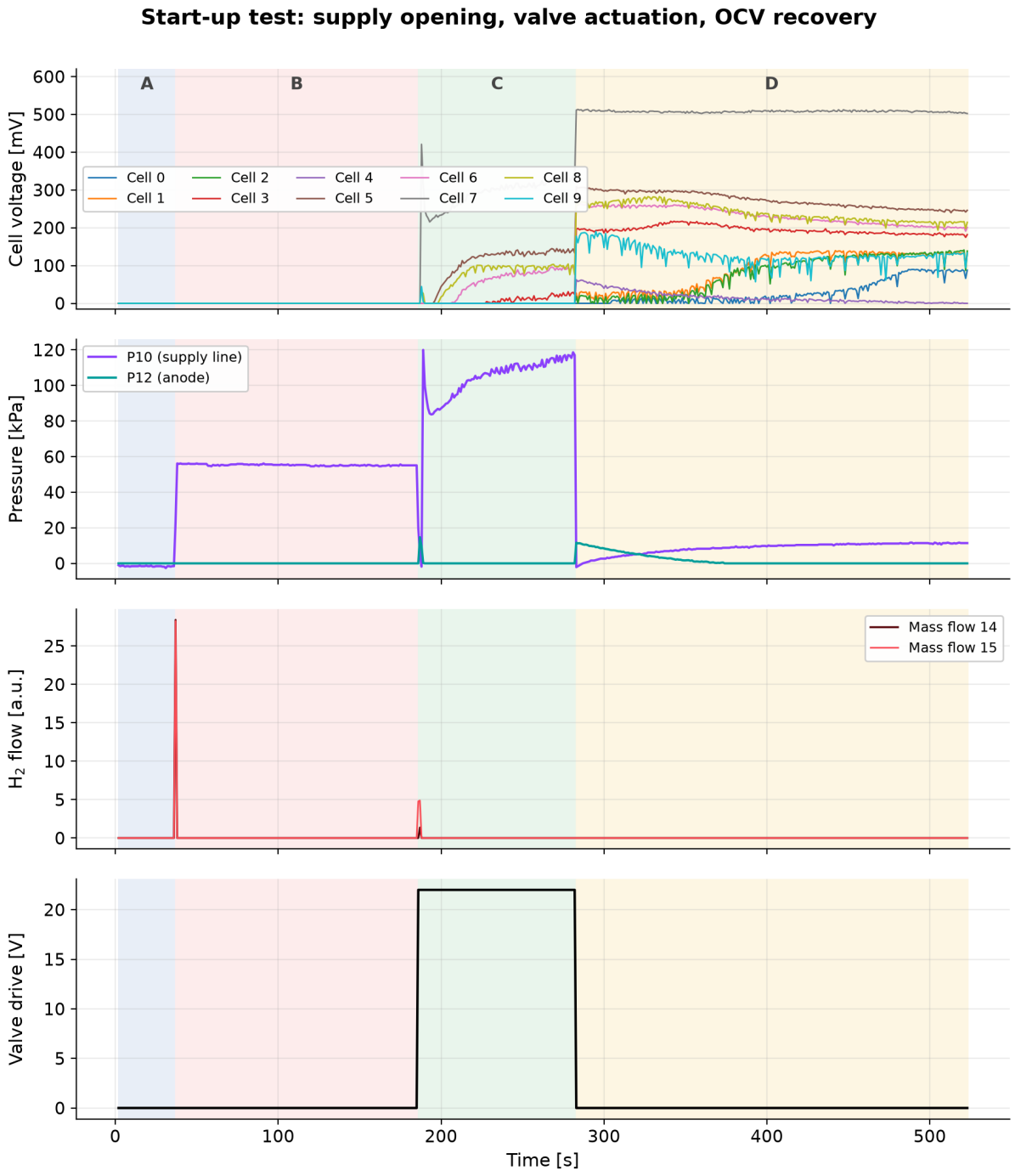


FIGURE 4.4: Start-up and valve test (7 July 2026). From top to bottom: cell voltages, hydrogen-circuit pressures, mass flow, and valve command. Stages: (A) everything closed; (B) supply regulator open, valve closed: no cell responds; (C) valve fully open: the anode fills and the cells wake up; (D) valve closed: OCV recovery on the trapped hydrogen.

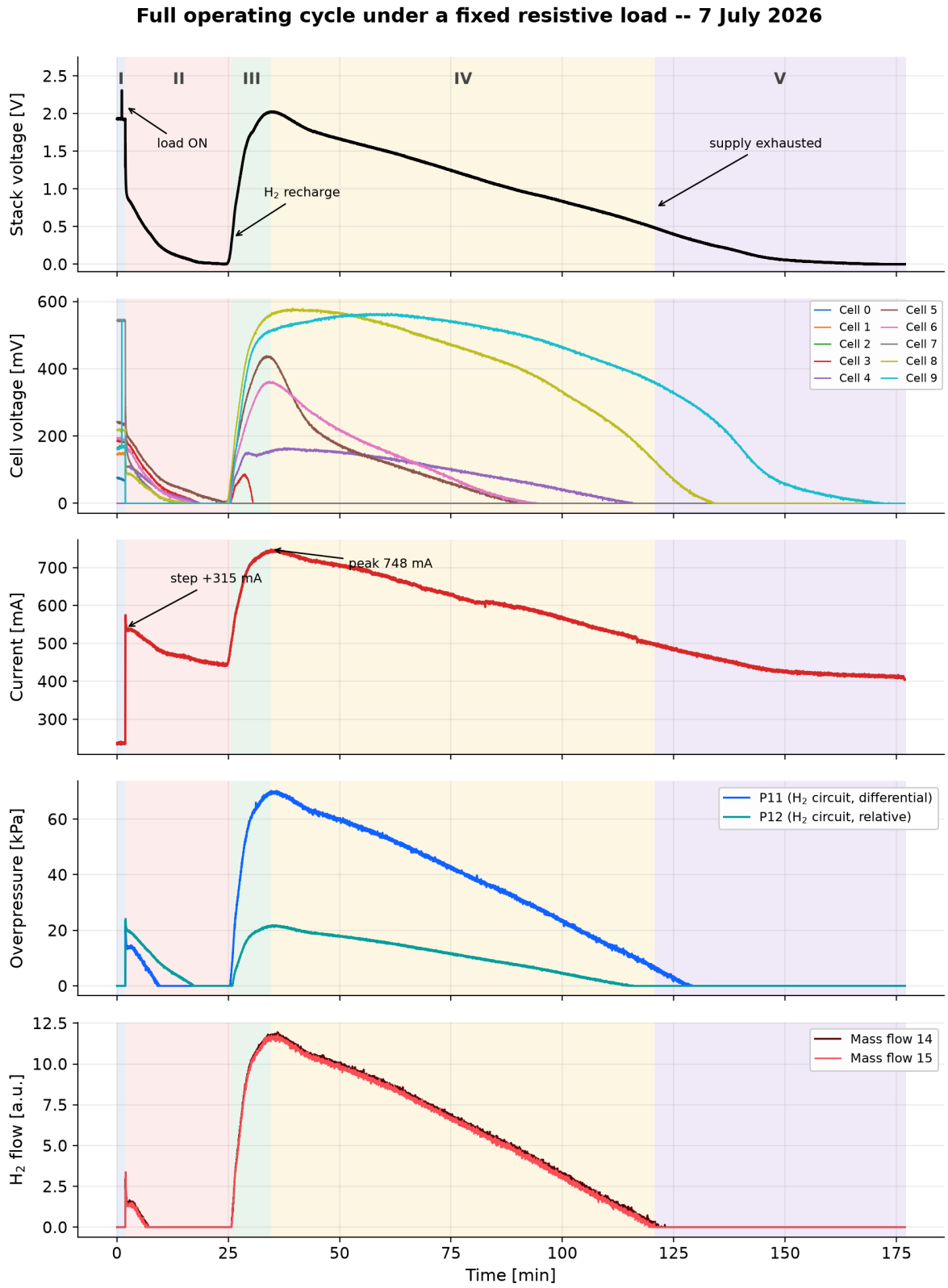


FIGURE 4.5: Full operating-cycle experiment (7 July 2026): stack voltage, per-cell voltages, load current, hydrogen-circuit overpressures (re-zeroed to their rest level), and mass flows across the five phases of Table 4.3. The brief voltage spike at load-ON coincides with a short hydrogen injection made at the connection instant. The current axis retains the original script's mA label; its gain and offset are uncalibrated.

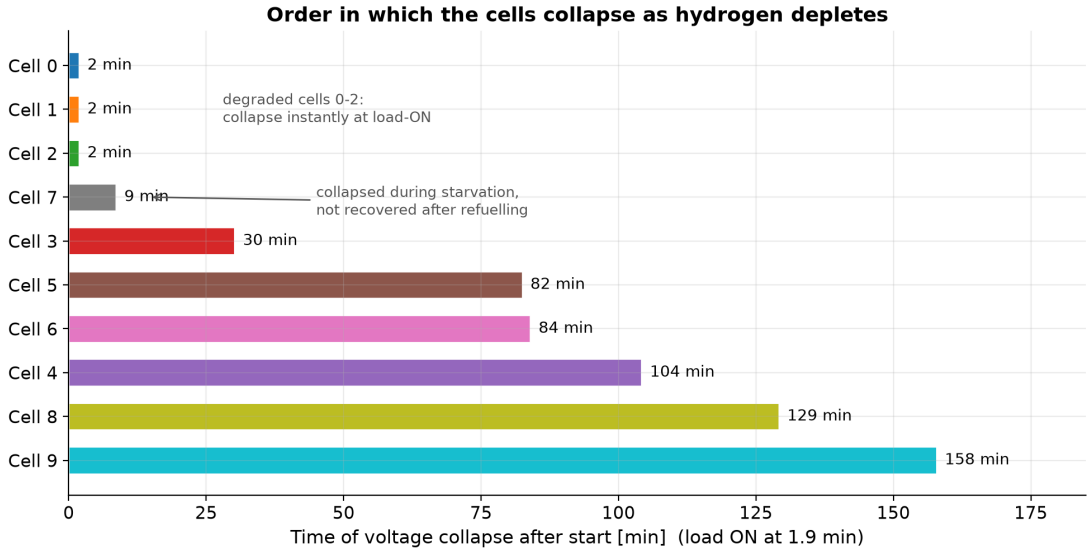


FIGURE 4.6: Time at which each cell's voltage collapses (below 30 mV for good) during the full operating-cycle experiment. The bar order ranks voltage-loss times under this protocol, not intrinsic health: cells 0–2 lose voltage at load-ON, cell 7 loses voltage during starvation and does not recover after refuelling, and other cells cross the threshold later.

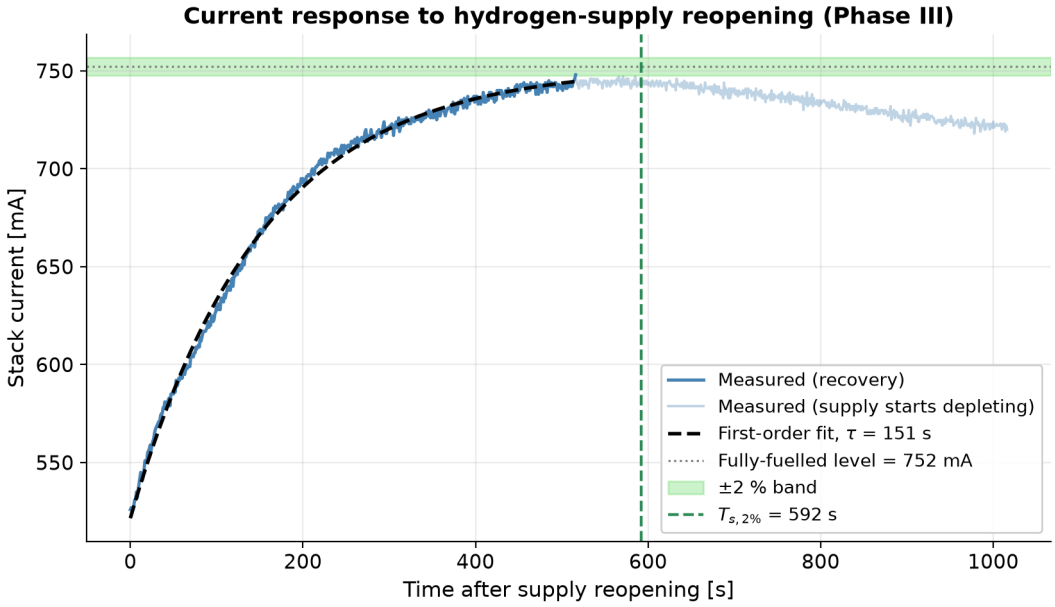


FIGURE 4.7: Current response to the hydrogen-supply reopening (Phase III of the full cycle), fitted with a first-order model over the recovery segment. The fitted supply-side time constant $\tau_s \approx 151$ s is more than an order of magnitude slower than the load-side constants of Table 4.2; beyond the peak, the slow depletion of Phase IV takes over (lighter trace). The ideal 2 % time extends beyond the fitted recovery segment, and the current scale is uncalibrated.

Chapter 5

Control of the PEMFC Power System: DC/DC Boost Converter with PI Controller

This chapter presents a proposed control architecture for the PEMFC power system. As motivated in Section 2.4.1, the limited authority of the hydrogen supply motivates control on the electrical side through a DC/DC converter. Missing stack-temperature and oxygen-side pressure sensors also limit model validation and state estimation: temperature and cathode oxygen partial pressure are assumed in the present calibration. This further motivates PI regulation using electrical current or voltage feedback, whose calibration remains necessary. The design follows Derbeli et al. [4]; no converter or closed-loop PI experiment is reported for the present bench.

5.1 System Overview

The PEMFC terminal voltage V_{STACK} varies with current and operating conditions. A DC/DC boost converter can shape this output, with a PI controller acting on its duty cycle d through pulse-width modulation (PWM). Figure 5.1 shows two possible objectives:

- **stack-current regulation**: the loop regulates the inductor (stack) current I_L to I_{REF};
- **output-voltage regulation**: the loop regulates the load-side voltage V_{OUT} to V_{REF}.

These objectives concern different terminals of the converter. Regulating I_L controls current drawn from the fuel cell, not directly the current delivered to the load.

5.2 Stack-Current Regulation

Following [4], the proposed design proceeds in five steps.

1) *Control objective.* The controlled variable is the inductor current I_L, which the PI loop forces to track I_{REF}. Derbeli et al. use 9.74 A at a simulated maximum-power point of 54 W and 5.54 V, and quote a 10 A limit for their stack. These are reference-system values, not ratings or setpoints established for the present bench. Its current reference and limits require separate hardware characterization.

2) *Boost converter state-space model.* For ideal components in continuous conduction, averaging over one PWM period gives, with $x = [\, i_L \; V_{OUT} \,]^\top$, load R, inductance L, and capacitance C:

$$\dot{x} = \underbrace{\begin{bmatrix} 0 & (d-1)/L \\ (1-d)/C & -1/(RC) \end{bmatrix}}_{A_b(d)} x + \begin{bmatrix} 1/L \\ 0 \end{bmatrix} V_{STACK}, \qquad y_i = \begin{bmatrix} 1 & 0 \end{bmatrix} x. \tag{5.1}$$

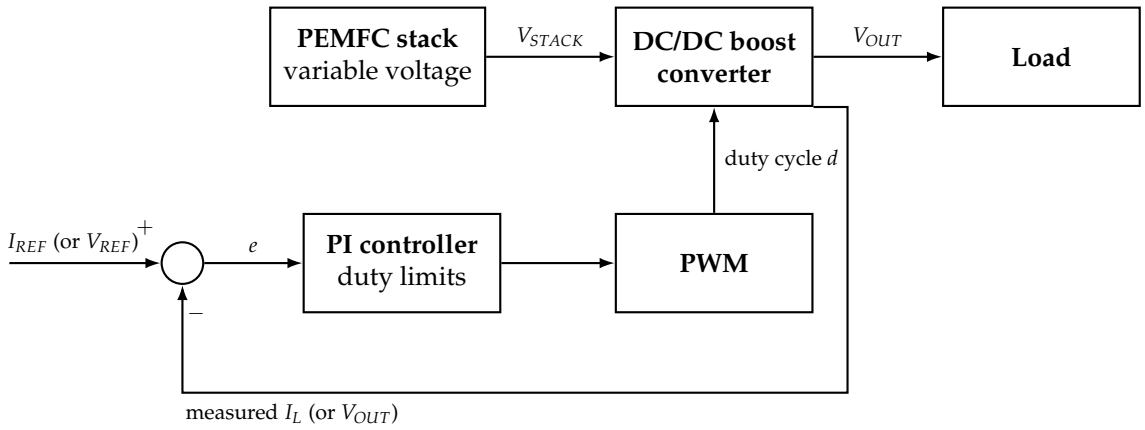


FIGURE 5.1: Proposed architecture after [4]. The current loop regulates the current drawn from the stack; the voltage loop regulates the load-side voltage. Duty limits and anti-windup remain to be implemented.

The voltage input is V_{STACK} and the manipulated variable is d; the averaged model is bilinear in duty and state. About a nominal condition (x_0, d_0), its duty-to-state mapping is

$$\delta\dot{x} = A_b(d_0)\delta x + \underbrace{\begin{bmatrix} V_{OUT,0}/L \\ -i_{L,0}/C \end{bmatrix}}_{B_d} \delta d + \begin{bmatrix} 1/L \\ 0 \end{bmatrix} \delta V_{STACK}. \tag{5.2}$$

This local model must ultimately be coupled to the stack voltage dynamics; it is not validated by the resistive-load fits alone.

3) *PI control law.* With $e = I_{REF} - I_L$, a conceptual duty command is

$$d = \mathrm{sat}_{[d_{min}, d_{max}]} \left(d_0 + K_P e + K_I \int e\, dt \right), \qquad 0 \le d_{min} < d_{max} < 1. \tag{5.3}$$

The proportional term shapes the response and integral action can remove steady error. Anti-windup is needed when duty saturates; current-reference limits and calibrated current feedback must also be specified. These implementation details remain pending.

4) *PI tuning.* Derbeli et al. describe an online procedure using an ultimate proportional gain K_{PU} and an integral time T_{iU}, setting $K_P = K_{PU}/2$ and $T_i = 2T_{iU}$, with $K_I = K_P/T_i$. No such bench tuning is claimed here. Converter components, sampling, admissible current, and the operating point must first be established; gains cannot be inferred from τ_I alone.

5) *Expected behavior.* The reference paper reports an approximately 400 ms simulated response at 9.74 A and separate dSPACE 1104 experiments at a 4 A reference [4]. These results motivate the architecture, without predicting its performance on the present stack. Tracking error, overshoot, settling, and load rejection remain to be measured after implementation.

The averaged capacitor balance makes the distinction between terminal currents explicit:

$$i_{OUT} = (1-d)i_L - C\dot{V}_{OUT}, \qquad i_{OUT,0} = (1-d_0)i_{L,0}. \tag{5.4}$$

Thus constant stack current does not by itself make the converter output an ideal current source when duty or load changes.

5.3 Output Voltage Regulation (Voltage-Source Operation)

Here the goal is a regulated load-side voltage, using the same PI structure. The loop forces V_{OUT} toward V_{REF} within the converter's feasible voltage and available stack power. Equations (5.1) and (5.2) apply with $y_v = \begin{bmatrix} 0 & 1 \end{bmatrix} x = V_{OUT}$. Set $e = V_{REF} - V_{OUT}$ in (5.3), retaining duty limits, anti-windup, and a separately enforced stack-current limit.

The voltage loop requires its own analysis and gains: its duty-to-voltage dynamics include the inductor, capacitor, load, and stack response. Current-loop tuning cannot simply be reused. Stack-current regulation controls the fuel-cell operating point, while voltage regulation serves a fixed-voltage load. Both remain proposed objectives, with bench-specific tuning and closed-loop validation still required.

Chapter 6

Conclusion & Perspectives

This work developed a simplified control-oriented model of a ten-cell PEMFC stack, calibrated it per cell on the Optimization Experiment, derived and analyzed its linearized state-space representation, characterized its dynamic current response to load steps and to the hydrogen supply, and proposed a PI-based control architecture for the PEMFC power system.

The main outcomes are: (i) a local empirical voltage fit with calibration RMSE below 12 mV for cells 3–9, whose coefficients are not separately identifiable as physical activation parameters; (ii) a two-coefficient comparison model with chronological holdout RMSE of 1.8–10.2 mV, giving a stronger within-run check while still using measured inputs; (iii) an analytical state-space model showing rank-one controllability from hydrogen inlet flow alone and incomplete observability from voltage, with pressure estimation conditional on known or fixed hydration; (iv) fitted load-step current time constants of approximately 8–10 s and ideal settling times of 32–40 s, with sensitivity to the fitting interval; (v) a proposed DC/DC boost converter with PI regulation of stack current or output voltage [4]; and (vi) a full operating-cycle experiment recording sequential loss of cell voltage and a supply-recovery time constant of about 151 s. The latter observations support further study of coordinated electrical and gas-supply control, without establishing a universal bandwidth ratio or an intrinsic cell-health ranking.

Perspectives follow directly. The first priority is to verify sensor gains and offsets, load values, and the low-voltage channels, then repeat measurements under documented fuel and hydration conditions. On the modeling side, the physical activation convention must be reconciled with the implementation and recalibrated. Independent experiments with varied excitation are needed to assess prediction, while validated water-removal terms are needed for a nonzero-current equilibrium. Oxygen transients and gas-supply delays [8] would further extend the model's validity.

On the control side, converter component selection, operating-point linearization, PI tuning, duty limits, and anti-windup must precede closed-loop assessment on this bench. Reference tracking and load disturbances should be evaluated together with stack-current limits and individual cell voltages. The approximately 400 ms response from the reference study is not a measured performance of this stack. Start-up and shutdown must follow the approved bench procedure; the present experiments do not justify attributing cell damage to open-circuit operation or prescribing a new load-first sequence.

Bibliography

[1] A. E. Andrea, M. Mañana, A. Ortiz, C. Renedo, L. I. Eguíluz, S. Pérez, and F. Delgado. A simplified electrical model of small pem fuel cell. *Renewable Energy and Power Quality Journal*, 1(4), 2006.

[2] Yan Cao, Yiqing Li, Geng Zhang, Kittisak Jermsittiparsert, and Navid Razmjooy. Experimental modeling of pem fuel cells using a new improved seagull optimization algorithm. *Energy Reports*, 5:1616–1625, 2019.

[3] WRW Daud, RE Rosli, EH Majlan, SAA Hamid, R Mohamed, and T Husaini. Pem fuel cell system control: A review. *Renewable Energy*, 113:620–638, 2017.

[4] Mohamed Derbeli, Maissa Farhat, Oscar Barambones, and Lassaad Sbita. Control of proton exchange membrane fuel cell (PEMFC) power system using PI controller. In *Proceedings of the International Conference on Green Energy Conversion Systems*. IEEE, 2017.

[5] GIPSA-lab. Infinity. https://www.gipsa-lab.grenoble-inp.fr/recherche/departement-automatique-et-surete-des-systemes-das/infinity/. Official team presentation. Accessed 22 October 2026.

[6] GIPSA-lab. Le laboratoire. https://www.gipsa-lab.grenoble-inp.fr/le-laboratoire/. Official laboratory presentation. Accessed 22 October 2026.

[7] V. Ionescu. Water and hydrogen transport modelling through the membrane-electrode assembly of a pem fuel cell. *Physica Scripta*, 95:034006, 2020.

[8] Jamil Kharrat and Jan Haußmann. Influence of the gas supply component delay on the dynamic operation of the PEM fuel cell system. In *Proceedings of the Hydrogen Technology Conference*, 2025.

[9] Y. B. Kim and S. J. Kang. Time delay control for fuel cells with bidirectional dc/dc converter and battery. *International Journal of Hydrogen Energy*, 35:8792–8803, 2010.

[10] A. K. M. Mohiuddin, N. Basran, and A. A. Khan. Modelling and validation of proton exchange membrane fuel cell (pemfc). *IOP Conference Series: Materials Science and Engineering*, 290:012026, 2018.

[11] Jay T. Pukrushpan. *Modeling and Control of Fuel Cell Systems and Fuel Processors*. PhD thesis, The University of Michigan, 2003.

[12] M. Shen and K. Scott. Power loss and its effect on fuel cell performance. *Journal of Power Sources*, 148:24–31, 2005.

[13] K. K. T. Thanapalan, J. G. Williams, G. P. Liu, and D. Rees. Modelling of a pem fuel cell system. In *Proceedings of the 17th IFAC World Congress*, 2008.

[14] A. Thomya and Y. Khunatorn. Design of control system of hydrogen and oxygen flow rate for proton exchange membrane fuel cell using fuzzy logic controller. In *Energy Procedia*, volume 9, pages 186–197, 2011.

[15] U.S. Department of Energy. Introduction to hydrogen for code officials: Text version. https://www.hydrogen.energy.gov/docs/hydrogenprogramlibraries/pdfs/introduction_to_hydrogen_for_code_officials_text_version.pdf. Hydrogen Program training materials, especially Hydrogen and Fuel Cell Basics, slides 5–6 and 16. Accessed 22 October 2026.

[16] U.S. Department of Energy. Safe use of hydrogen. https://www.energy.gov/cmei/fuels/safe-use-hydrogen. Accessed 22 October 2026.

[17] Yuhang Wang, Haotian Li, Huimin Feng, Kuihua Han, Suoying He, and Ming Gao. Simulation study on the pemfc oxygen starvation based on the coupling algorithm of model predictive control and pid. *Energy Conversion and Management*, 249:114851, 2021.

[18] Adam Z. Weber and John Newman. Modeling transport in polymer-electrolyte fuel cells. *Chemical Reviews*, 104(10):4679–4726, 2004.

[19] G. Zhang, L. Fan, J. Sun, and K. Jiao. A 3d model of pemfc considering detailed multiphase flow and anisotropic transport properties. *International Journal of Heat and Mass Transfer*, 115:714–724, 2017.

[20] Yun Zhu, Jianxiao Zou, Chao Peng, Yucen Xie, and Liying Li. Modelling and fuel flow control of pemfc considering over-pressure case. In *Proceedings of the IEEE Conference on Industrial Electronics and Applications*. IEEE, 2017.

Appendix A

Derivation of the Open-Circuit Voltage

The global hydrogen–oxygen reaction is $\mathrm{H_2} + \tfrac{1}{2}\mathrm{O_2} \rightarrow \mathrm{H_2O}$. At non-standard conditions the Gibbs free energy change is

$$\Delta g_f = \Delta g_f^0 - \bar{R} T_{fc} \ln\left(\frac{p_{H_2}\, p_{O_2}^{1/2}}{p_{H_2O}}\right),$$

and for a reversible cell $\Delta g_f = -2FE$, so

$$E = -\frac{\Delta g_f^0}{2F} + \frac{\bar{R} T_{fc}}{2F} \ln\left(\frac{p_{H_2}\, p_{O_2}^{1/2}}{p_{H_2O}}\right).$$

Standard Voltage

Taking liquid water as the product at 25 °C:

$$E^0 = -\frac{\Delta g_f^0}{2F} = -\frac{-237{,}200}{2 \times 96{,}485} \approx 1.229 \text{ V}.$$

Table A.1 lists Δg_f^0 at several temperatures.

TABLE A.1: Gibbs free energy change of the hydrogen fuel cell reaction at various temperatures [11].

Product	Temperature (°C)	Δg_f^0 (kJ/mol)
Liquid	25	−237.2
Liquid	80	−228.2
Gas	80	−226.1
Gas	100	−225.2
Gas	200	−220.4
Gas	600	−199.6
Gas	1000	−177.4

Temperature Coefficient

From $\Delta G^0 = \Delta H^0 - T\Delta S^0$, with

$$\Delta S^0 = S^0_{\mathrm{H_2O(l)}} - S^0_{\mathrm{H_2(g)}} - \tfrac{1}{2} S^0_{\mathrm{O_2(g)}} = 69.95 - 130.7 - 102.58 \approx -163.3 \text{ J mol}^{-1}\text{K}^{-1}$$

for the liquid-water reaction,

$$\frac{\Delta S^0}{2F} \approx \frac{-163.3}{192{,}970} \approx -0.85 \times 10^{-3} \text{ V K}^{-1}.$$

Nernst Pressure Correction

Assuming $p_{H_2O} = 1$ (liquid product):

$$\frac{\bar{R}T_{fc}}{2F}\ln\!\left(p_{H_2}\,p_{O_2}^{1/2}\right) = \frac{8.314\,T_{fc}}{192{,}970}\left[\ln p_{H_2} + \tfrac{1}{2}\ln p_{O_2}\right] \approx 4.31\times10^{-5}\,T_{fc}\left[\ln p_{H_2} + \tfrac{1}{2}\ln p_{O_2}\right].$$

Final Expression

Combining all terms yields Equation (3.1) of the main text:

$$E = 1.229 - 0.85\times10^{-3}(T_{fc} - 298.15) + 4.31\times10^{-5}\,T_{fc}\left[\ln p_{H_2} + \tfrac{1}{2}\ln p_{O_2}\right]\ \text{V}.$$

Appendix B

Detailed Tables

TABLE B.1: Fitted coefficients and calibration RMSE for all ten cells (Optimization Experiment). Cells 0–2 collapsed under load: the optimizer returns identical degenerate parameter sets that reproduce a near-zero voltage and are not physically meaningful. At fixed temperature and oxygen concentration, the individual activation coefficients are non-unique (Section 3.2).

Cell	RMSE [mV]	ξ_1	ξ_2	ξ_3	ξ_4	B	c
Cell 0†	0.08	-7.783	1.67×10^{-2}	-6.06×10^{-4}	≈ 0	1.08×10^{-2}	1.00×10^{-2}
Cell 1†	0.08	-7.783	1.67×10^{-2}	-6.06×10^{-4}	≈ 0	1.08×10^{-2}	1.00×10^{-2}
Cell 2†	0.08	-7.783	1.67×10^{-2}	-6.06×10^{-4}	≈ 0	1.08×10^{-2}	1.00×10^{-2}
Cell 3	4.66	-1.977	2.83×10^{-2}	1.32×10^{-3}	-3.17×10^{-4}	≈ 0	≈ 0
Cell 4	2.18	0.386	1.43×10^{-2}	8.11×10^{-4}	-1.24×10^{-4}	≈ 0	≈ 0
Cell 5	4.23	0.682	3.00×10^{-2}	1.93×10^{-3}	-2.98×10^{-4}	≈ 0	≈ 0
Cell 6	4.51	1.775	4.62×10^{-3}	4.87×10^{-4}	-2.73×10^{-4}	≈ 0	≈ 0
Cell 7	5.62	1.796	2.54×10^{-2}	1.82×10^{-3}	-1.99×10^{-4}	≈ 0	≈ 0
Cell 8	1.96	-4.946	2.81×10^{-2}	6.92×10^{-4}	-1.34×10^{-4}	≈ 0	≈ 0
Cell 9	11.25	-5.400	2.01×10^{-2}	9.31×10^{-5}	-1.06×10^{-4}	3.21×10^{-7}	≈ 0

† Abnormal loaded voltage; fit not physically meaningful.

These values reproduce the original optimizer output and its implemented sign convention. They are not independent measurements of material or electrode properties. Correcting the physical activation convention requires a new calibration and corresponding replacement of the fitted curves.

Appendix C

Source Code

The complete source code developed during this internship is available on GitHub. It gathers the simplified PEMFC model, the per-cell parameter-identification scripts (differential evolution + L-BFGS-B), the experiment-processing and figure-generation pipelines, and the LaTeX sources of this report and of the defense presentation:

https://github.com/KhalilEllahLAGHA/PEMFC_Internship_codes

The chronological holdout and consistency checks are available in `Analysis/verify_experiments.py`, alongside the report sources in `Report/Fuel cell modeling and controlling Report`. The required Python packages are listed in `Analysis/requirements.txt`.

Appendix D

Additional Processing and Prediction Checks

D.1 Per-Cell Calibration and Reconstruction

The two per-cell grids support the quantitative discussion in Section 4.1. They are gathered here to keep the body focused on the experiment-level results and their interpretation.

D.2 Calibration and Reconstruction Windows

The Optimization Experiment contains 1081 samples from $t = 0$ to 1080 s. The detected loaded interval contains 549 samples, $t = 135$–683 s. Removing the first 164 samples (30 %, rounded down) leaves 385 samples from $t = 299$ to 683 s; the original calibration uses 80 uniformly selected rows. Its reconstructed current is 16.00–25.84 mA and its assumed absolute hydrogen pressure is 1.2961–1.3652 atm. These pressure values follow the existing parser's gauge-to-absolute conversion and require the sensor calibration to be correct. The assigned constants are $T = 343.15$ K, $p_{O_2} = 0.21$ atm, $\lambda_m = 14$, $A_{fc} = 25 \times 10^{-4}$ m^2, $t_m = 178 \times 10^{-6}$ m, and $i_{\max} = 0.25$ A. They are modeling settings, not newly measured quantities.

TABLE D.1: Calibration error and full-loaded-interval reconstruction error using the original fitted coefficients. Reconstruction includes the excluded transient.

Cell	3	4	5	6	7	8	9
Calibration RMSE [mV]	4.66	2.18	4.23	4.51	5.62	1.96	11.25
Loaded RMSE [mV]	3.61	7.46	4.34	3.89	31.71	6.00	16.15

The unweighted mean loaded RMSE over cells 3–9 is 10.45 mV; the corresponding mean over all ten channels is 8.01 mV. Stack reconstruction RMSE is 45.54 mV. These are different metrics and should not be interchanged. The open-circuit reconstruction separately fits a per-cell effective temperature to unloaded measurements; its 811–1468 K range is empirical and has no thermometric interpretation.

D.3 Chronological Holdout

The comparison model in (4.1) is fitted only to the first 269 settled samples ($t = 299$–567 s). The remaining 116 samples ($t = 568$–683 s) are withheld. Pressure ranges are 1.3158–1.3652 atm for training and 1.2961–1.3158 atm for holdout, while current ranges overlap. The log-current coefficient is unconstrained and empirical: the exercise tests local prediction rather than identifying a physical activation mechanism. Neither block is an independent experiment, and current is reconstructed from the measured voltage sum, so the inputs are not independent of the outputs. The last included sample, $t = 683$ s, contains a voltage/current rise just before detected resistor removal and materially increases the reported errors. It is retained in the primary assessment. As an endpoint sensitivity check only, excluding that row gives holdout RMSEs of 1.22, 1.57, 1.44, 1.41, 5.71, 1.20, and 4.16 mV for cells 3–9 respectively; these do not replace the primary results.

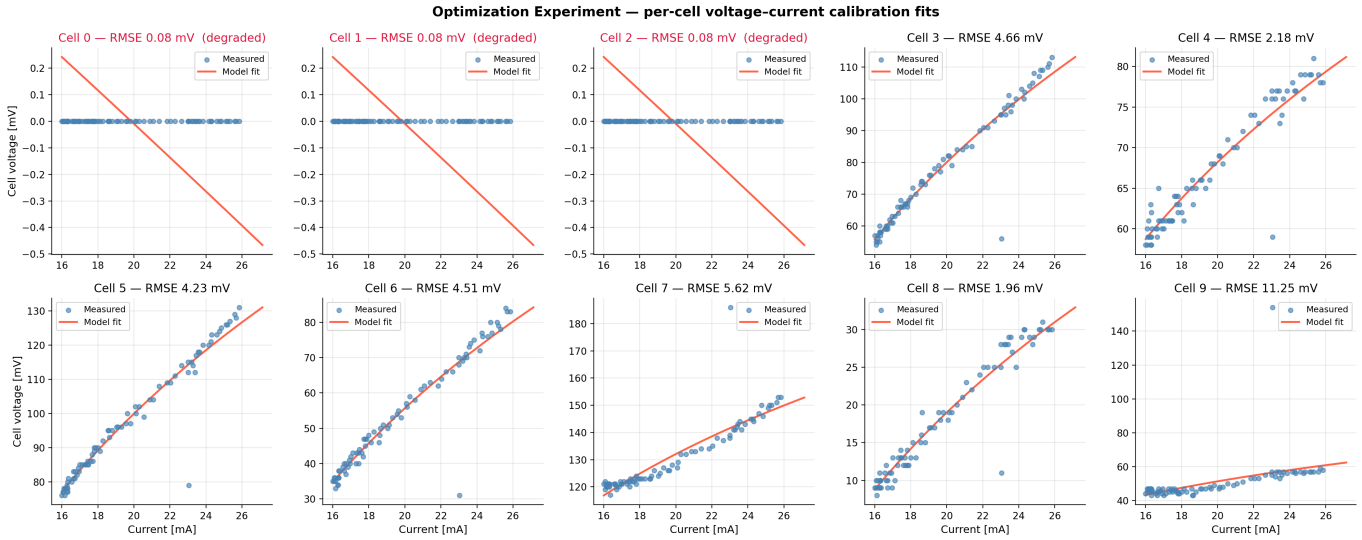


FIGURE D.1: Per-cell voltage–current calibration fits: measured points (blue) versus the empirical model (red). Cells 3–9 have calibration RMSE between 2.0 and 11.3 mV. Cells 0–2 approach zero voltage under load and their fitted coefficients have no physical interpretation. Voltage collapse alone does not identify the failure mechanism.

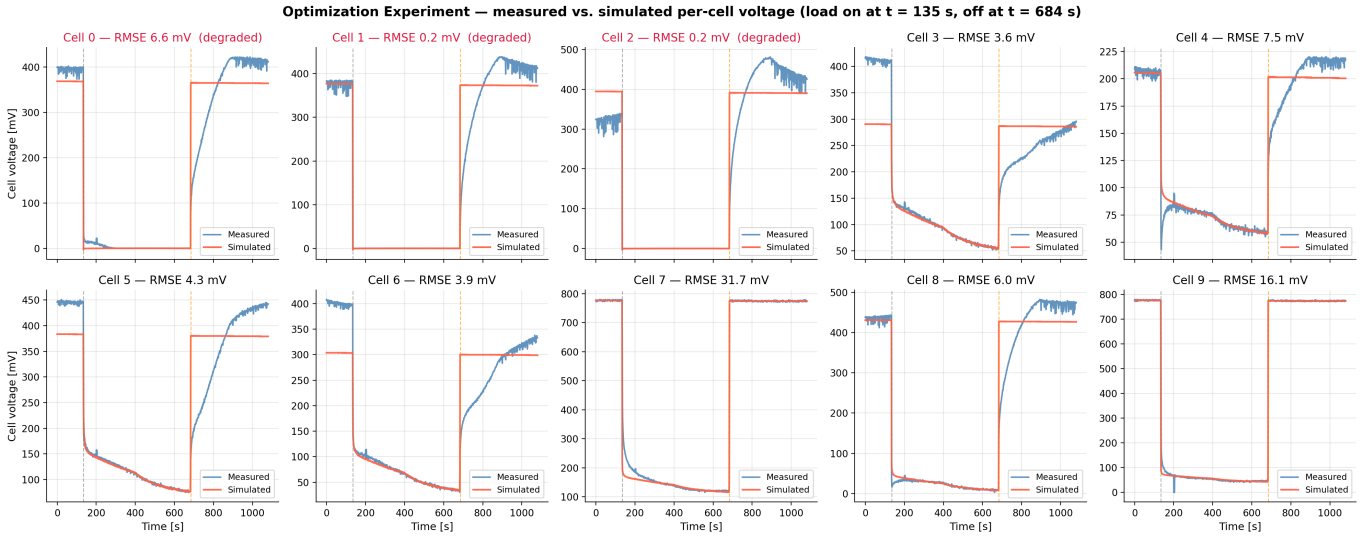


FIGURE D.2: Per-cell voltage, measured (blue) versus reconstructed (red), over the experiment. Titles report loaded-window RMSE (mean 10.5 mV for cells 3–9). Measured pressure and reconstructed current are inputs; the red open-circuit segments are fitted separately.

D.4 Current-Response Fits and Measurement Provenance

For the datasets labelled 3.3 and 6.8 Ω, the whole-record fits use $t = 0$–250 and 0–175 s respectively. The fitted asymptotes are 576.38 and 557.68 on the scripts' mA scale, whereas the last-20 % means are 572.92 and 556.06. A curve fitted with a free asymptote must use that same asymptote when constructing its ideal settling band. The revised figure therefore uses $I_{ss,\mathrm{fit}} \pm 0.02|\Delta I_{\mathrm{fit}}|$. Measurement noise and slow drift can keep individual samples outside the band after the ideal time. The whole-record fit RMSEs are 3.78 and 2.08 on the recorded current scale.

The processed TR files label the raw current channel as mA. Its gain and zero offset are not independently established by those files; the July processing explicitly acknowledges an open-circuit offset of about 237 counts. The recorded voltage-to-current ratios also do not directly match the nominal resistor labels. This does not identify whether the discrepancy comes from load notes, voltage conversion, current gain, or current offset. It prevents using the absolute current and power values as calibrated measurements until these quantities are checked. A constant affine sensor conversion preserves the time constant of an ideal exponential; drift or nonlinear conversion need not preserve it.

The July voltage processing uses 0.905108432 mV per count, while the earlier tagged-log parser uses the voltage values as already expressed in mV. These different conventions must be verified against the acquisition firmware rather than silently merged. All revised checks retain the original conventions and state their limitations.

D.5 Reproducibility

The revised project includes `Analysis/verify_experiments.py`, numerical CSV/JSON outputs, and the regenerated figures. The verification script reads the existing raw logs and fitted-coefficient file without changing them. It records input hashes, processing windows, fitting choices, and package versions. These additional checks do not replace an independently calibrated experiment or a closed-loop test of the proposed converter.

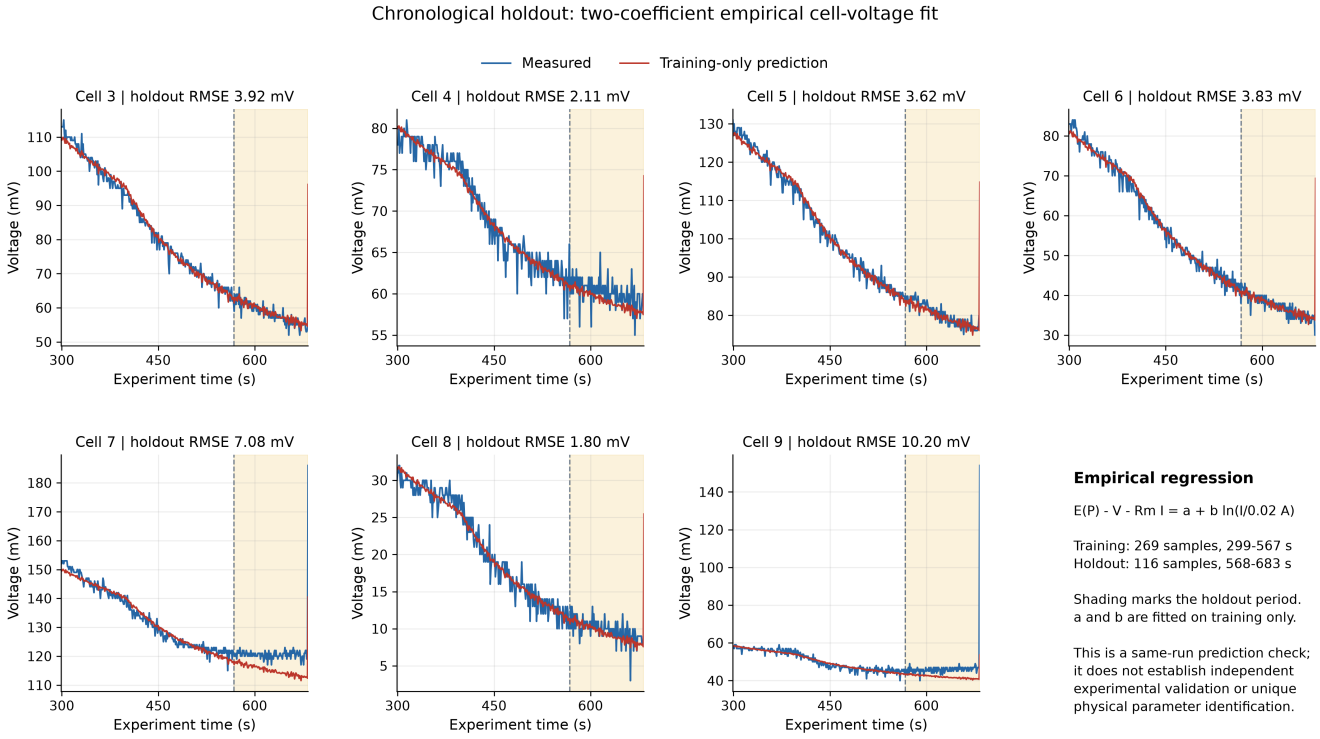


FIGURE D.3: Chronological holdout for cells 3–9. The vertical division separates the samples used to fit the two empirical coefficients from those withheld for assessment. No holdout voltage is used to fit the coefficients; measured pressure and reconstructed current remain inputs in both blocks.